J. Fluid Mech. (2012), *vol.* 701, *pp.* 59–97. © Cambridge University Press 2012
doi:10.1017/jfm.2012.132

Interaction of a strong shockwave with a gas bubble in a liquid medium: a numerical study

N. A. Hawker and Y. Ventikos†

Department of Engineering Science, University of Oxford, Parks Road, Oxford OX1 3PJ, UK

(Received 13 February 2011; revised 1 March 2012; accepted 5 March 2012)

The interaction of a shockwave with a gas bubble in a liquid medium is of interest in a variety of areas, e.g. shockwave lithotripsy, cavitation damage and the study of sonoluminescence. This study employs a high-resolution front-tracking framework to numerically investigate this phenomenon. The modelling paradigm is validated extensively and then used to explore the parametric space of interest. We provide a comprehensive qualitative analysis of the collapse process, which we categorize into three phases, based on the principal feature dominating each phase. This results in the characterization of numerous previously unidentified features important in the evolution of the process and in the emergence of peak temperatures and pressures. For example, we discover that the peak pressure does not occur as a result of the impact of the main transverse jet (also called the re-entrant jet) but later in the collapse. We perform fully three-dimensional simulations, showing that three-dimensional instabilities are limited to the small-scale details of collapse, and continue by comparing collapse of cylindrical and spherical bubbles. We detail a parametric investigation varying the shock strength from 100 MPa to 100 GPa. A counter-intuitive discovery is that the maximum gas density decreases with increasing shock strength.

Key words: bubble dynamics, shock waves, sonoluminescence

1. Introduction

The collapse of a cavity or bubble can be observed in various physical situations, both in nature and technology. Understanding of non-spherical collapse, more specifically that characterized by the formation of a main transverse jet (also called the re-entrant jet), is less well developed than corresponding understanding of spherical collapse. The most fully researched situation involving this type of non-spherical bubble collapse involves an inertially collapsing bubble in the presence of a solid boundary. It is known that two bubbles oscillating in phase with one another feel an attractive Bjerknes force and begin to move towards each other (Bjerknes 1906; Pelekasis & Tsamopoulos 1993*a*,*b*; Kröninger *et al.* 2010). Near a rigid wall the bubble effectively interacts with its mirror image, giving the fluid around the bubble a certain amount of momentum towards the wall. As the bubble collapses the only way this momentum can be conserved is through deformation of the surface from spherical, leading to the development of a high-speed jet directed into the bubble in the direction of the wall (Benjamin & Ellis 1966; Plesset & Prosperetti 1977; Philipp & Lauterborn 1998). Cavitation erosion, where a solid surface is damaged by nearby

† Email address for correspondence: yiannis.ventikos@eng.ox.ac.uk

https://doi.org/10.1017/jfm.2012.132 Published online by Cambridge University Press

collapsing bubbles, has been observed for nearly a century (Cook 1928; Kornfeld & Suvorov 1944) and is an important field of engineering and design, directly relating to non-spherical bubble collapse. The damage is generally known to occur through two mechanisms. First, the strong shockwaves generated by the bubble collapse can interact with the surface. This interaction was first modelled for a spherical collapse (Rayleigh 1917) but it is now known that non-spherical collapse is the more prevalent mechanism. The strong shocks are understood to be caused by the impact of the emerging high-speed jet on the opposite bubble wall (Plesset & Chapman 1971; Lauterborn & Bolle 1975; Ball *et al.* 2000). The second mechanism occurs when the bubble is in very close proximity to or attached to the wall. This leads the jet to impact the wall directly, causing 'erosion by water hammer' (Cook 1928; Plesset & Prosperetti 1977). This second mechanism is understood to be the more potent one (Philipp & Lauterborn 1998).

Recent development in cavitation damage research has involved increasingly better resolved experimental observations and data about the collapse of cavitation bubbles (Brujan *et al.* 2002; Lindau & Lauterborn 2003; Wang & Chen 2007) as well as several numerical studies of the problem (Klaseboer *et al.* 2007; Johnsen & Colonius 2008, 2009). One little understood phenomenon in this type of non-spherical collapse is the formation of a 'counter-jet' that emerges moving away from the wall (Philipp & Lauterborn 1998; Lindau & Lauterborn 2003). The driving mechanism of this is not determined with certainty; however Lindau & Lauterborn (2003) theorize that it is not part of the original bubble but results from the emergence of cavitation: a region of low pressure develops as the various shockwaves generated by the collapse propagate outwards. This would fit with the lack of observation of the counter-jet in numerical work since to include cavitation would require explicit, non-trivial additions to utilized computational methodologies.

A second prominent situation giving non-spherical collapse is the interaction of a bubble with a shockwave and it is on this that we focus our study. Although the driving mechanism is different, the dynamics of collapse are qualitatively similar in that a portion of the bubble wall involutes and forms a high-speed jet (Mader 1965). However, the evolution of a counter-jet, as observed for collapse near a wall, is not recorded in this case. Shock–bubble interaction has several notable applications, including the sensitization of explosives and shockwave lithotripsy. It has been known for some time that the presence of cavities within an explosive can provide a means for accelerating or initiating impact detonation (Bowden & Gurton 1948; Mader 1965; Coley & Field 1973). Bourne (2002) reviews three possible mechanisms for this behaviour, namely, viscous heating in the liquid of the main transverse jet, compression of the gas trapped between the jet tip and the bubble wall and bulk compression of the bubble. Initial theory assumed a spatially uniform compression within the bubble but the dominant mechanism heating the gas inside the bubble is now known to be shock compression (Ball *et al.* 2000), although as we shall see this is still a broad generalization of the rich dynamics that occur. High temperatures have been observed directly by Bourne & Field (1999) in the form of luminescence. In fact, two temporally distinct flashes of luminescence are observed corresponding roughly to jet impact and compression of the subsequently toroidal bubble, interpretations supported further by numerical investigations (Bourne & Milne 2003). Thus, they conclude that the second and third heating mechanisms are the most important. Shockwave lithotripsy uses shockwaves to non-invasively break down stones in the body and it is thought that the interaction of the generated pressure pulse with bubbles near the stone causes the stone to fragment via similar mechanisms to

https://doi.org/10.1017/jfm.2012.132 Published online by Cambridge University Press

cavitation erosion (Kodama & Tomita 2000; Arora, Junge & Ohl 2005; Klaseboer *et al.* 2007; Johnsen & Colonius 2008; Leighton *et al.* 2008).

Another well-investigated phenomenon involving bubbles is sonoluminescence, where oscillating bubbles in a liquid collapse and emit light (Frenzel & Schultes 1934). This is now understood to be caused by the formation of plasma in the bubble (Suslick, Doktycz & Flint 1990; Flannigan & Suslick 2005) that is most probably caused by an imploding shockwave generated by the supersonic motion of the bubble wall (Mellen 1956; Hiller, Putterman & Barber 1992; Wu & Roberts 1993). Sonoluminescence can occur in a single, stable bubble (single-bubble sonoluminescence – SBSL) (Gaitan *et al.* 1992; Matula & Crum 1998; Brenner, Hilgenfeldt & Lohse 2002) or within a transient cloud of multiple bubbles (multi-bubble sonoluminescence – MBSL) (Hansson, Kedrinskii & Morch 1982; McNamara, Didenko & Suslick 1999; Didenko & Gordeychuk 2000). For SBSL it is generally assumed that the bubble remains spherical during the collapse (Moss *et al.* 1994; Yasui 1997; Nigmatulin *et al.* 2005), although in the final moments this is not necessarily the case (Barber *et al.* 1997; Prosperetti 1997). In MBSL the situation is more complex. When a sonoluminescing bubble approaches its minimum volume a strong outward water-hammer shock is created, hence shock–bubble interactions will be taking place in the MBSL cloud. It is clear that greater understanding of the fundamentals of non-spherical collapse will have implications for this field (Lauterborn & Kurz 2010). Sonoluminescence has attracted attention due to the level of energy focusing it demonstrates (Weninger, Camara & Putterman 1999) and this has found various applications both tangible, such as sonochemistry (Suslick 1990; Thompson & Doraiswamy 1999; Suslick & Flannigan 2008), and controversial, such as sonofusion (Shapira & Saltmarsh 2002; Taleyarkhan *et al.* 2002). The intense conditions created by shock-driven bubble collapse could well prove to have the same potential for exploitation.

Analytical and numerical modelling of bubble collapse began with analysis of spherical collapse by Rayleigh (1917), which has since been extended by various authors (Plesset 1949; Gilmore 1952; Keller & Miksis 1980). However, shock-driven collapse of a cavity in a liquid has defied concise analytical treatment, which leaves numerical methods as the foremost means of shedding light on complex experimental observations and of enhancing our understanding of the situation. Unfortunately it is also substantially non-trivial from a numerical point of view; in fact it has become a test case for the most cutting-edge compressible flow methods (Ball *et al.* 2000; Nourgaliev, Dinh & Theofanous 2006; Chang & Liou 2007; Turangan *et al.* 2008). The dynamics of the problem are entirely dominated by the motion and interaction of the discontinuities in the flow (i.e. shockwaves, rarefactions and the gas/liquid contact), the complexity of which increases drastically when examining the flow regime after the high-speed jet impact. Dealing with these discontinuities poses a difficult challenge to numerical methods: unsophisticated methods tend to be overly diffusive or generate large unphysical oscillations in the solution. The boundary integral method (Plesset & Chapman 1971; Klaseboer *et al.* 2007), based on potential flow, allows the interface to be clearly resolved but is fundamentally an incompressible model. It can provide insight into the initial stages of collapse but is unable to reliably progress beyond the point of jet impact. To resolve the dynamics robustly a compressible approach must be employed. Ding & Gracewski (1996) used an arbitrary Lagrangian–Eulerian (ALE) approach and set out to perform a parametric study of shock strength. Their focus was partly on the comparison to the spherical collapse models. The results for weak shockwaves proved satisfactory but the resolution achievable was not sufficient

https://doi.org/10.1017/jfm.2012.132 Published online by Cambridge University Press

to model strong shockwaves, the result being that important dynamics were not pursued (given the computational resources of the time). More recent work for weak shockwaves (up to ∼60 MPa) can be found in Johnsen & Colonius (2008, 2009). They use a weighted essentially non-oscillating (WENO) scheme with an implementation of the Harten, Lax and van Leer solver with contact restoration (HLLC). This successfully prevents any numerical oscillations about the shockwave or the liquid–gas contact. However, the contact line itself is spread over ∼4 grid cells which will inevitably blur some detail. This methodology can certainly be used for higher shock intensities, where the collapse geometry is more complex, but greater spatial resolution would be required. To look at high-strength shocks, Ball *et al.* (2000) and Turangan *et al.* (2008) employed a 'free-Lagrangian' code that uses an unstructured Lagrangian grid. For two-dimensional (2D) simulations, this uses quadrilaterals and for rotationally symmetric simulations it uses hexagons. The interface is resolved sharply by keeping the adjacent grid cells aligned with it. The propagation is then achieved with three different Riemann solvers: one for air/air cell boundaries, one for air/water and one for water/water.

The obtained resolution of this work has now been surpassed but the insight into the physical processes achieved still corresponds to what is probably the most definitive presentation of the process to date. Inevitably however, even this exposition is less detailed for the stages after jet impact. As mentioned above, general descriptions such as 'shock compression' overlook particularly complex and rich behaviour. We will return to this work in § 3.1. Nourgaliev *et al.* (2006) uses a modified level-set method to resolve the gas/liquid interface and an adaptive mesh refinement (AMR) algorithm, and Chang & Liou (2007) uses a modified advection upstream splitting method plus (AUSM+) scheme. These particularly sophisticated methods generate very impressive results; however the focus is on the development of the methodology itself and not on furthering the understanding of the fluid dynamics involved. Aiming at methodology development, they simulate a single case with the aim of validation rather than performing any parametric studies. Finally, work by Takahira, Matsuno & Shuto (2008) is of interest because they model a liquid medium other than water, examining strong shock–bubble interaction in mercury.

All the results cited here have common limitations in that they just model Euler's equations and do not perform fully three-dimensional (3D) simulations. Another significant challenge that is largely unaddressed for shock–bubble interaction is providing an equation of state that can accurately represent the bubble contents at the intense conditions that occur. As luminescence is observed, a true model of the gas in the bubble must be able to describe the formation of plasma. We have found only one study that stands out in this aspect of the modelling, including the present work, where the Chemkin II suite was utilized (Bourne & Milne 2003).

In this paper we aim to investigate in greater depth the fundamental mechanisms of shock–bubble interaction throughout the whole collapse process, including the difficult-to-resolve emerging patterns after the impact of the jet. The bulk of the analysis characterizing the various stages of shock–bubble interaction is presented in § 3.1, where a base case of 1 GPa shock and 1 mm bubble diameter is used. We aim to understand the physics of the collapse and to provide a set of terminology to effectively describe the various aspects. In § 3.2 we will present fully 3D simulations to look for any 3D effects in the flow and to compare spherical and cylindrical bubbles. Finally we perform a parametric study over incident shock strength in § 3.3. To achieve this we shall use a high-accuracy front-tracking scheme, which will be described in § 2.

https://doi.org/10.1017/jfm.2012.132 Published online by Cambridge University Press

As a small aside before we progress, this study focuses on a gas bubble in a liquid medium but there are similar studies of shock interaction with a gas bubble in a medium that is also gaseous. There has been a variety of work providing experimental insight and numerical modelling of this problem (Haas & Sturtevant 1987; Quirk & Karni 1996; Johnsen & Colonius 2006; Niederhaus *et al.* 2008; Ranjan *et al.* 2008) as well as some analytical work based on the baroclinic vorticity generation on the interface (Samtaney, Ray & Zabusky 1998; Ray, Samtaney & Zabusky 2000).

2. Numerical methodology

2.1. *Front tracking*

As discussed, the complex interplay of flow discontinuities makes numerical modelling of shock–bubble interaction a challenge. An essential requirement is a mechanism to resolve the gas–liquid contact. There are various methodologies available, such as volume of fluid (VOF) (Hirt & Nichols 1981), level set (Sethian 1999), marker particles (Harlow & Welch 1965) or front tracking (Glimm & McBryan 1985; Tryggvason 2001). Each has its advantages and disadvantages; for instance VOF requires no explicit code to deal with bifurcations in the flow but implementing surface tension is non-trivial (Brackbil, Kothe & Zemach 1992). For this study we use a front-tracking code, *FronTier*, originally developed by Glimm & McBryan (1985) and since worked on by numerous authors (Glimm *et al.* 1981; Glimm 1988; Glimm *et al.* 1988; Grove 1994; Li 1996; Glimm 1998; Glimm *et al.* 1998, 1999; Glimm, Grove & Zhang 2002; Haller *et al.* 2002; Glimm *et al.* 2003; Du *et al.* 2006; Liu *et al.* 2007; Xu *et al.* 2007; Fix *et al.* 2008; Jiao & Zha 2008; Lu *et al.* 2008). We chose *FronTier* because its accuracy compares very favourably with other methodologies (Du *et al.* 2006), it is capable of resolving the interface down to subgrid levels (Fix *et al.* 2008) and it has been implemented for fully 3D simulations (Glimm *et al.* 1998).

The essence of front tracking is the use of a lower-dimensional Lagrangian grid to represent a discontinuity in the flow (Glimm 1998). This is overlaid on an underlying Eulerian grid that is used with a hyperbolic solver to model the bulk flow away from the discontinuities. For 2D simulations the Lagrangian grid (or 'front') is a piecewise linear curve, whereas for 3D it is a surface constructed from triangles. The algorithm must account for the coupling between the propagation of the front and the update of the states in the bulk flow between the fronts. Hence each point on a front has two associated thermodynamic states, one on either side, and thus a time step proceeds in two stages.

First the fronts are propagated in two steps, normal and tangential. The normal is calculated using the weighted least-square polynomial fitting (WLSP) algorithm developed by Jiao & Zha (2008). A stencil is then filled using the states on the front itself plus states interpolated from the underlying Eulerian grid and the front states. This is used with Riemann problem methods to calculate both the velocity of the point on the front, and hence its new position, and the updated front states (Glimm *et al.* 1986, 1999, 2002). The tangential update allows waves to propagate along the length of the front. Thus for each point there are two tangential updates, one on either side. There is no need to update the positions in this step (Glimm *et al.* 1981). In 3D there are two tangential steps in orthogonal directions, giving four per point. The state is updated using the same hyperbolic solver as the bulk states. As a natural consequence of propagation the points on the front will tend to diverge or converge, leading to a poorer quality representation, and thus a 'redistribution' algorithm is required (Du *et al.* 2006). Also, intersections must be correctly identified and an

https://doi.org/10.1017/jfm.2012.132 Published online by Cambridge University Press

'untangle' algorithm must then act appropriately. In *FronTier*, this problem has been very comprehensively addressed for a contact discontinuity in both 2D (Glimm *et al.* 1988) and 3D (Glimm *et al.* 2000).

Secondly the states in the bulk flow are updated, solving Euler's equations,

$$\frac{\partial \boldsymbol{q}}{\partial t} + \boldsymbol{\nabla} \cdot f(\boldsymbol{q}) = \boldsymbol{0}, \quad \boldsymbol{q}(\boldsymbol{x}, t) = \begin{pmatrix} \rho \\ \rho \boldsymbol{u} \\ E \end{pmatrix}, \quad f(\boldsymbol{q}) = \begin{pmatrix} \rho \boldsymbol{u} \\ \rho \boldsymbol{u}\boldsymbol{u} + p\boldsymbol{I} \\ (E + p)\boldsymbol{u} \end{pmatrix}, \tag{2.1}$$

where ρ is density, $\boldsymbol{u}$ is the flow velocity, E is the specific internal energy, t is time, $\boldsymbol{x}$ is the spatial coordinate, $\boldsymbol{\nabla}$ is the vector differential operator del and $\boldsymbol{I}$ is the identity matrix.

To perform this update an implementation of the MUSCL solver (van Leer 1979) is employed. The slopes are constructed as described by van Leer (1977) with the additional slope limiter described by Colella (1985). The Riemann solver used is an implementation of an exact solver. To perform 2D and 3D calculations Strang splitting is used (Glimm *et al.* 2002) and the time step is adaptively chosen to satisfy the Courant–Friedrichs–Lewy (CFL) condition (Courant, Friedrichs & Lewy 1967). The fronts act as moving boundary conditions for the hyperbolic solver. That is to say, when updating a point on one side of a front no information from the other side is used; the required values are found by interpolating/extrapolating from the underlying grid and the relevant points on the front (Glimm *et al.* 1999). The hyperbolic step has two steps: a 'regular sweep' updating cells away from fronts and an 'irregular sweep' updating those near (Glimm *et al.* 2002).

In this study we use front tracking to resolve the motion of the contact line between the gas and the liquid; the shockwaves are captured adequately by the underlying hyperbolic solver, being spread over ∼2 grid cells. This methodology, and in particular results obtained through this front-tracking technique, have been used successfully by the authors in the past to investigate problems where liquid–gas interfaces and the compressibility of both phases are dominant (Haller *et al.* 2002; Haller, Ventikos & Poulikakos 2003; Haller *et al.* 2003). Grid independence results are presented in § A.1 in the appendix and validation results are presented in § A.2.

2.2. *Equation of state*

Another important aspect of modelling compressible fluids is the equation of state. Throughout the study we work with both air and water and hence we need two equations of state. Since front tracking splits the domain into separate regions the inclusion of two different equations is straightforward. The air is modelled with the ideal-gas equation. This is very accurate at normal pressures and temperatures but as the conditions intensify it becomes diminishingly suitable. It provides no modelling of effects such as dissociation and ionization and, since these processes will absorb energy from the system, temperatures are likely to be over-predictions and to be regarded as only semi-quantitative (Ball *et al.* 2000). However, when properly validated (see § A.2 in the Appendix) the ideal-gas modelling allows understanding of the mechanisms involved and prediction of trends (Ball *et al.* 2000).

The modelling of water in previous works has evolved around two equations of state, the Tait equation (Ball *et al.* 2000; Turangan *et al.* 2008) or the stiffened polytropic equation (Nourgaliev *et al.* 2006; Takahira *et al.* 2008). These are incomplete equations of state; the Tait equation provides no means to calculate temperature and the standard stiffened polytropic equation produces temperatures that are very

https://doi.org/10.1017/jfm.2012.132 Published online by Cambridge University Press

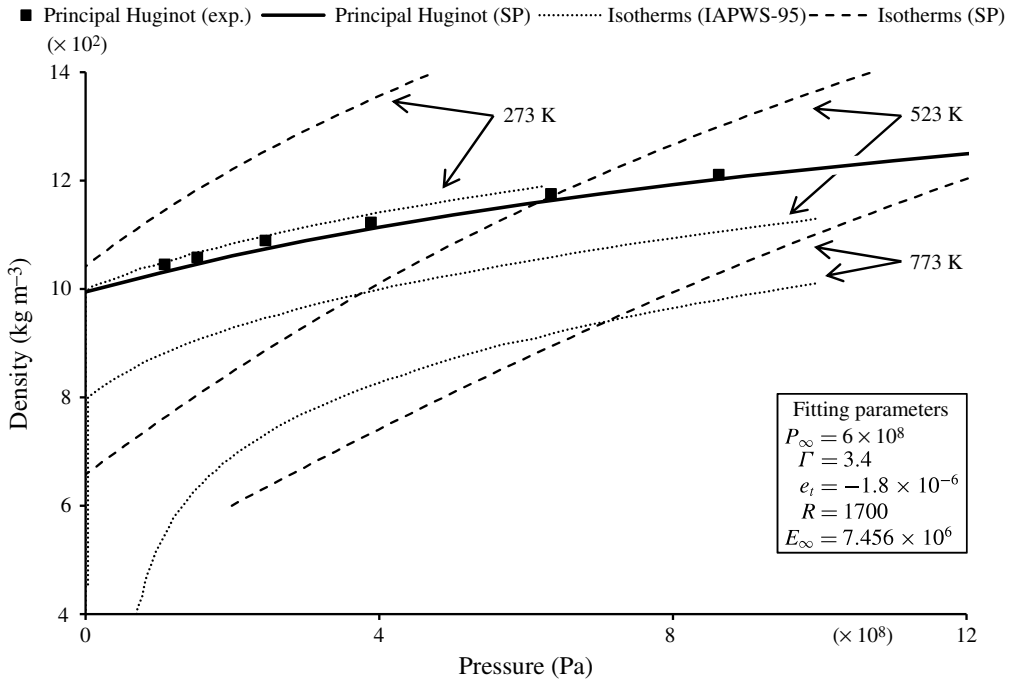


FIGURE 1. Fitting of the modified stiffened polytropic equation of state given in (2.2) to experimental data (Nagayama *et al.* 2002) and IAPWS-95 (Wagner & Pruss 2002). Given the simplicity of the equation of state, the agreement achieved is deemed very satisfactory.

inaccurate. Here we use the following complete version of the stiffened polytropic equation, with two extra parameters to renormalize the values for temperature and internal energy (Menikoff & Plohr 1989):

$$p + (\Gamma + 1)\, P_\infty = \Gamma \rho\, (e + E_\infty)\,, \quad RT = \frac{(p + P_\infty)}{\rho} + \Gamma e_t \rho^\Gamma\,, \tag{2.2}$$

where p is the pressure, T is the temperature, ρ is the density, e is the specific internal energy, P_∞ is the stiffened pressure constant, Γ is the Grueneisen exponent, R is the gas constant, e_t is the thermal energy factor and E_∞ is the energy translation factor.

Since we are looking at a shock-dominated problem we chose the values of the parameters to fit experimental data for the principal Hugoniot of water (Nagayama *et al.* 2002) first and foremost. We then ensured that the density at standard pressure and temperature was accurate and finally we tried to fit the isotherms to the IAPWS-95 equation of state (Wagner & Pruss 2002). Figure 1 shows the results of this fitting and the values that we used. We can see that the shock behaviour is well captured and that the isotherm trends are correct. The parameter E_∞ is involved only in the determination of internal energy and was fitted such that the internal energy is zero at the triple point.

2.3. *Problem initialization*

To conclude this section we present some problem-specific details. In order to validate our work against the available experimental data we model a cylindrical bubble; however in § 3.2 we extend the analysis to both axisymmetric and full 3D results. A reflecting boundary is used such that only half a bubble is modelled, thus halving

https://doi.org/10.1017/jfm.2012.132 Published online by Cambridge University Press

the number of grid cells required. For the full 3D simulations presented in § 3.2 no reflected boundary is used; a full spherical bubble is modelled. Both models have been constructed such that there are little to no boundary effects on the bubble. When we refer to bubble sizes we are discussing the diameters and the bubbles are initialized at rest and in equilibrium with the surrounding water, i.e. at standard temperature and pressure. The shockwave is initially planar and normal to the reflecting boundary. The pressure behind it is modelled as constant.

3. Results and discussion

3.1. *Characterizing the non-spherical collapse process*

We stated in § 1 our belief that the description of collapse dynamics given by Ball *et al.* (2000) is the authoritative presentation for a strong shock. Hence before we look at our own results we present a short summery of their observations. When the shock strikes the bubble it produces a strong expansion fan and a transmitted shock in the gas. As the flow evolves the bubble wall involutes and forms a high-speed and accelerating jet, which drives a strengthening of the transmitted shock. The water shock continues to propagate and near to the bubble it becomes weakened, thus becoming curved. As the jet and gas shock cross the bubble, the gas shock forms a regular reflection with the bubble wall and eventually reflects along the shock's entire length. The jet impacts the far bubble wall and a high-pressure 'blast wave' is created, whilst the reflected gas shock interacts with the side of the jet. As the flow evolves the blast wave propagates outwards and the gas shock develops a converging shape, eventually creating another compression wave in the liquid. Finally the bubble remains are drawn into the core of the vortex ring created from the jet impact.

Our first aim is to elucidate in more detail these collapse dynamics and, as we shall see, we discover a layer of detail unresolved by previous work. For example, there is more than one distinct shock present within the bubble that influences the dynamics. To do this we will follow figures 2–16, which show the collapse of a 1 mm bubble by a 1 GPa shockwave. Supplementary material is also provided showing animations of the collapse (available at journals.cambridge.org/flm). The right-hand side visualizes the raw data using the magnitude of the gradient of density, giving a 'numerical Schlieren' image, and the left-hand side presents a diagrammatic representation of the most important features, where the position of the bubble wall is given exactly by the raw front-tracking data. In this way we can label the features accordingly without obfuscating the original data. The times shown are zeroed at the first contact of the incident shock with the bubble.

To understand the non-spherical collapse process, where the initial bubble symmetry is primarily broken by the formation of the main transverse jet (also called the re-entrant jet), we have categorized the process into three phases. In each phase a single factor dominates the dynamics. In the first phase the dominant factor is the incident shock resulting in a reflected rarefaction and then the main transverse jet. The second phase is dominated by the outward-moving water-hammer shock and expelled gas shock, both generated by the impact of the main transverse jet on the downstream bubble wall, and in the final phase the motion is dictated by the leftover vortex ring. We have not explored every small feature that is present; we only discuss those features that appear across all shock strengths and bubble sizes and also manifest themselves in 2D, rotationally symmetric and 3D simulations. Thus we develop a set of terminology that can be used to compare and understand different collapse situations. In some cases we have renamed phenomena identified in other work. We

https://doi.org/10.1017/jfm.2012.132 Published online by Cambridge University Press

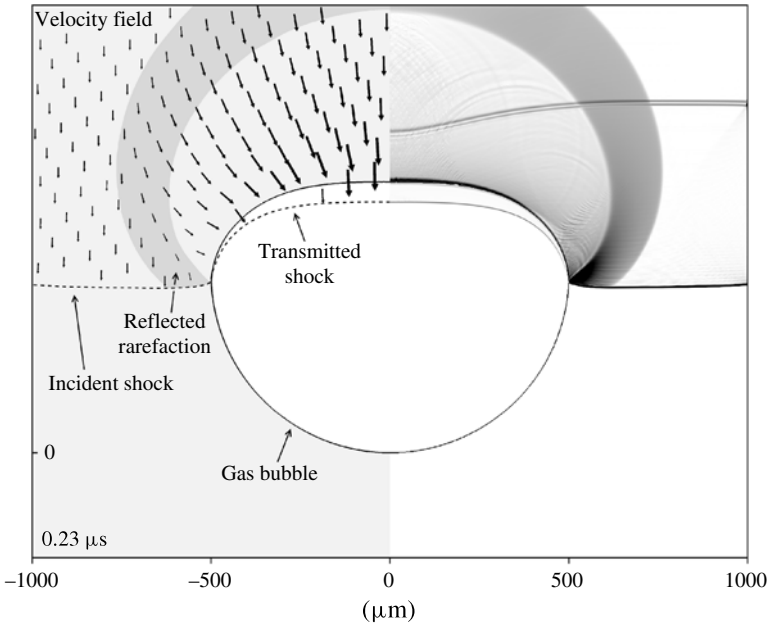


FIGURE 2. First phase: frame one. This is the first of a series of pictures depicting the collapse of a 1 mm diameter cylindrical bubble driven by a 1 GPa incident shock. The right-hand side plots the magnitude of the gradient of density to give a numerical Schlieren plot and the left-hand side gives a diagrammatic representation of the structures in the flow with corresponding labels, where the position of the gas/liquid contact is given exactly by the front-tracking data. The times shown are zeroed at the first contact of the incident shock with the bubble. The figures are discussed in § 3.1.

have done this so that the names reflect more information about the physical origin of the phenomena of interest.

3.1.1. *The first phase: incident shock*

When the incident shock first interacts with the upstream bubble wall it results in a reflected rarefaction, a bubble wall with a non-zero velocity and a transmitted shock. This configuration occurs because the acoustic impedance of the air is less than that of the water (Nourgaliev *et al.* 2006); were the converse true we would see a reflected shock rather than a rarefaction. As the interaction progresses the waves take on the configuration as shown in figure 2 (first phase: frame one). Here we see the anomalous reflection configuration reported by Grove & Menikoff (1990), where the leading edge of the reflected rarefaction has broken away from the bubble and is moving along the incident shock. This acts to weaken and bend the incident shock, as reported but not discussed by Ball *et al.* (2000). Plotting the velocity field illuminates very clearly the mechanism by which the main transverse jet is formed. Although this is not a complex mechanism it has not, to the best of our knowledge, been explicitly reported in previous work. The reflected rarefaction relaxes the pressure, which accelerates the flow. The curved shape causes this acceleration to focus the flow to a point on the upstream bubble wall, eventually causing it to involute and form the main transverse jet, as shown in figure 3 (first phase: frame two). The high velocity of this jet ($\sim$2000 m s^{-1}) drives the formation of a bow shock. The bow shock (pressure = 3.75 MPa, temperature = 2050 K) is significantly stronger than

https://doi.org/10.1017/jfm.2012.132 Published online by Cambridge University Press

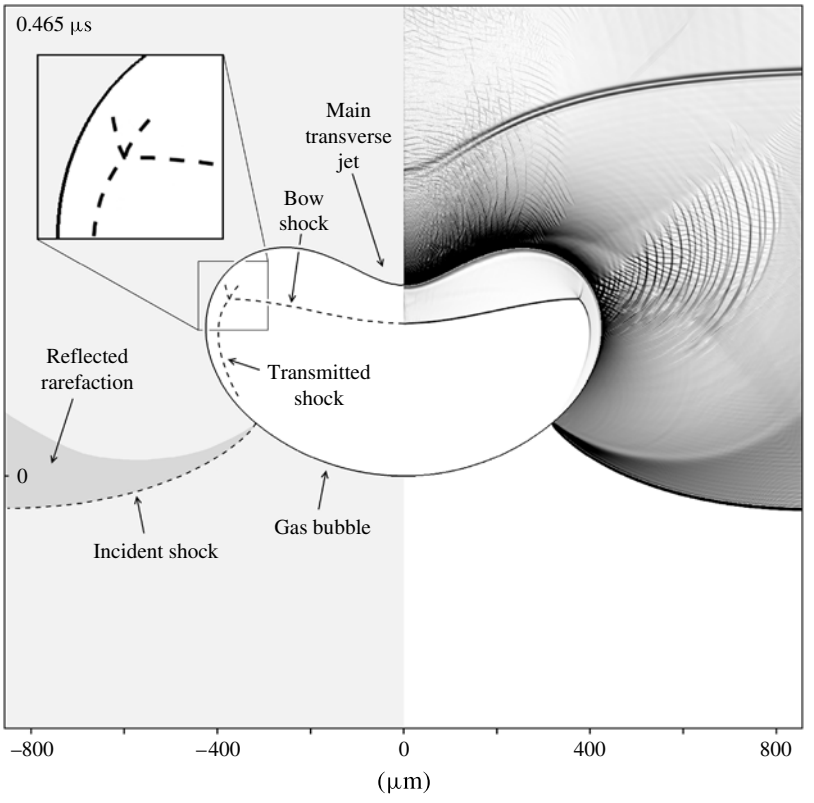


FIGURE 3. First phase: frame two.

the transmitted shock (pressure = 1.50 MPa, temperature = 991 K) and, as we can see in figure 3, dominates it. Previous work has not resolved this distinction between the transmitted shock and the bow shock. In figure 4 (first phase: frame three) we can see the bow shock regular reflection forming at the sidewall of the bubble. This, as shown in figure 5 (first phase: frame four), evolves into a complex configuration that still involves the bow-shock regular reflection but also includes structures that resemble a Mach reflection resulting from interaction with the transmitted shock. To neatly classify such interactions quickly becomes extremely difficult, a problem that we will see throughout. The final image of the first phase, figure 6 (first phase: frame five), depicts the situation after the bow shock has reached the far side of the bubble, resulting in the reflected bow shock, which moves back into the bubble, and the transmitted bow shock in the liquid (previously labelled the precursor shock (Johnsen & Colonius 2009)). The shock structure at the bubble wall appears like a Mach reflection but it is not; the reflected bow shock is moving back into the bubble and hence it is not directly interacting with the wall. In the inset we see the interaction of the reflected bow shock with the main transverse jet, forming the re-reflected bow shock. These rebounds provide a significant source of heating and compression in the bubble (the reflected bow shock is ∼4600 K and the re-reflected bow shock is ∼7700 K). The jet impact, which traps some gas between itself and the bubble wall, adds to this compression. Bourne & Field (1999) links the jet strike to the first flash of luminescence; here we have added more detail to the mechanism by which this occurs. An alternative source of this luminescence could be fractoluminescence of the water

https://doi.org/10.1017/jfm.2012.132 Published online by Cambridge University Press

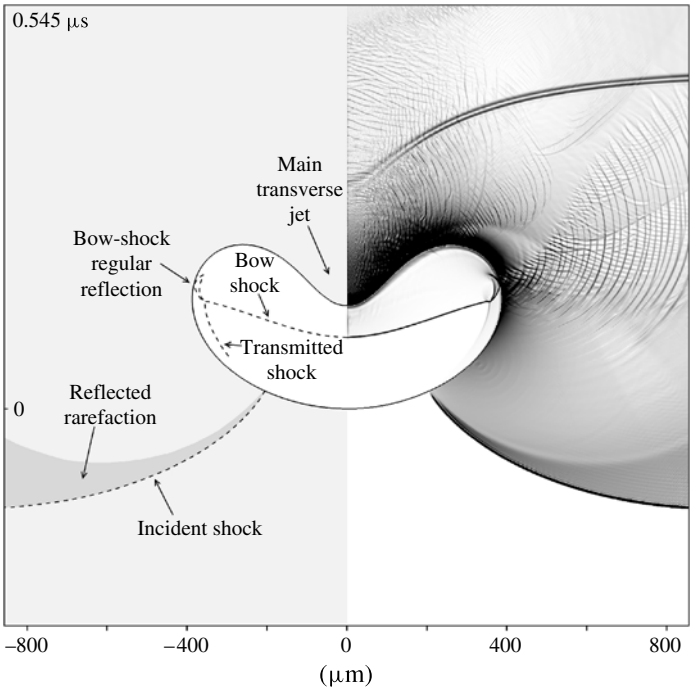


FIGURE 4. First phase: frame three.

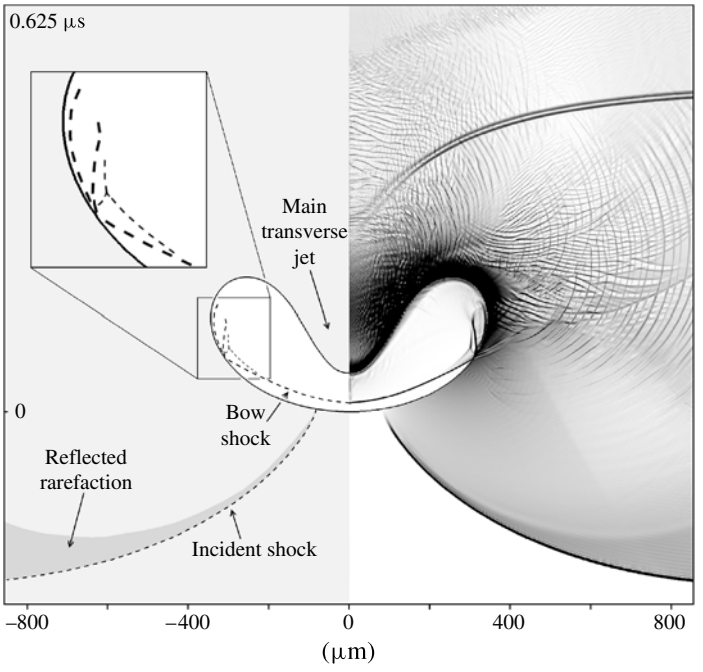


FIGURE 5. First phase: frame four.

https://doi.org/10.1017/jfm.2012.132 Published online by Cambridge University Press

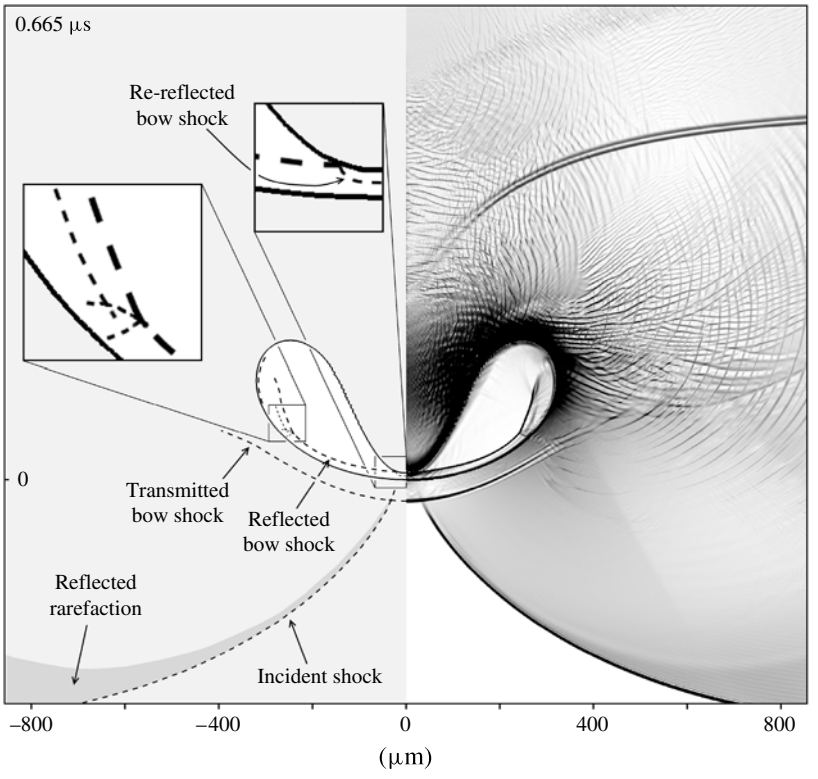


FIGURE 6. First phase: frame five.

directly impacted by the main transverse jet (Prosperetti 1997). Both mechanisms are possible, but these simulations reveal that distinguishing the two experimentally would be extremely difficult, since they are markedly close, temporally and spatially.

It might be expected (based on the study of gas–gas shock–bubble interactions) that the baroclinic vorticity deposited along the bubble wall by the incident shock would have an effect on the dynamics of the first phase. We find that the strength of the vorticity is insufficient to cause anything more than small ripples on the edges of the main jet.

In these first images there is an anomalous feature that appears as two black bars on the numerical Schlieren plots. This is a small trough in density caused by the initialization of the shockwave. The effect of this feature on the rest of the dynamics is minimal if present at all.

3.1.2. *The second phase: water hammer shock*

We define the second phase to begin when the main transverse jet strikes the downstream bubble wall, as shown in figure 7 (second phase: frame one). As is well known, the impact generates a very strong water-hammer shock (also called the 'blast wave', Ball *et al.* 2000; Johnsen & Colonius 2009). We find that this can be up to 10 times the pressure of the incident shock (see § 3.3.3). This mechanism is particularly noteworthy due to its potential importance in MBSL. In the case of a 1 GPa incident shock the water-hammer shock is ∼3 GPa. Since the water-hammer

https://doi.org/10.1017/jfm.2012.132 Published online by Cambridge University Press

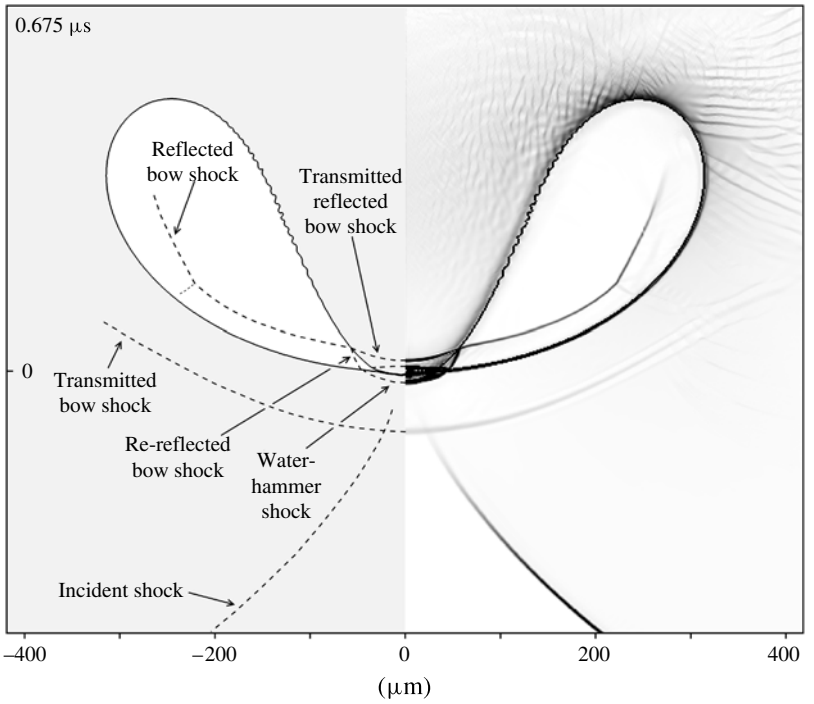


FIGURE 7. Second phase: frame one.

shock is the dominant force in the second phase, yet its strength entirely depends on the dynamics of the first phase, its pressure is a good way to quantify the overall collapse intensity. We can also see the re-reflected bow shock and transmitted reflected bow shock close in by the region of the impact. The impact itself is not the only powerful mechanism at the beginning of the second phase, the gas underneath the tip of the jet is expelled at very high velocity ($\sim$4000 m s^{-1}), forming the expelled-gas shock (pressure = 0.132 GPa, temperature = 8720 K). This can be seen in detail in the inset in figure 8 (second phase: frame two) where we can see the expelled-gas shock has also been transmitted into the water on either side, giving the transmitted expelled-gas shock. This expelled-gas shock can be seen in previous work (Chang & Liou 2007) but it has not been identified or discussed. By the next image, figure 9 (second phase: frame three), the expelled-gas shock and transmitted expelled-gas shock have dominated the remaining influence of the re-reflected and transmitted bow shocks.

Figure 9 also shows the beginning of an important process we shall see throughout the second phase: the formation and unstable breakdown of secondary, toroidal sheet jetting. This is visible in various published results (Bourne & Milne 2003; Chang & Liou 2007) and is labelled as a 'secondary jet' by Nourgaliev *et al.* (2006); however its consequences, including its role in the formation of the peak pressures and temperatures, has not been explored. The sheet jetting is driven by the water-hammer shock in a manner different from the way the main transverse jet is driven by the incident shock. The main transverse jet is created by the reflected rarefaction focusing the flow; there is no such corresponding rarefaction created by the water-hammer shock. The main transverse jet strikes the leeward bubble wall and divides the bubble

https://doi.org/10.1017/jfm.2012.132 Published online by Cambridge University Press

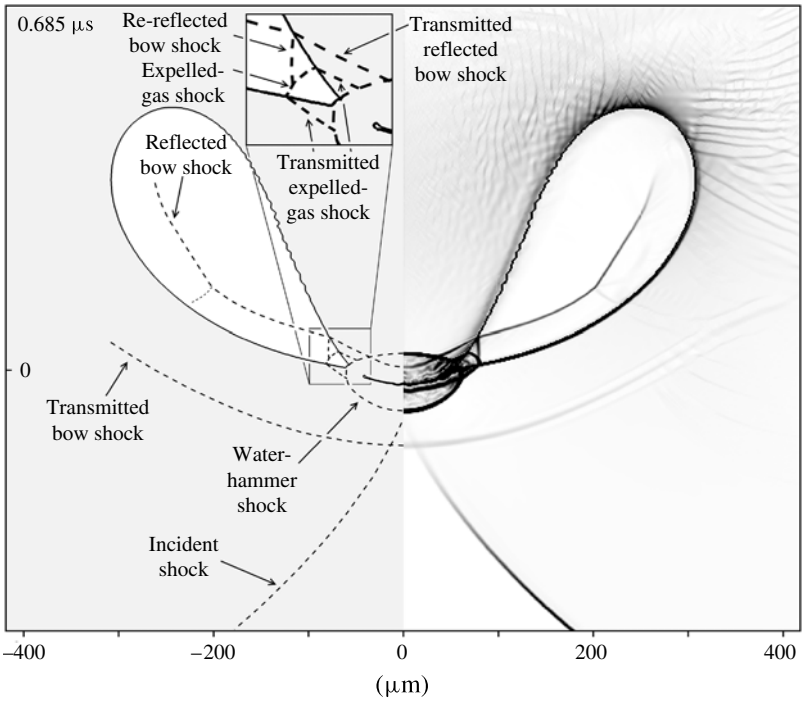


FIGURE 8. Second phase: frame two.

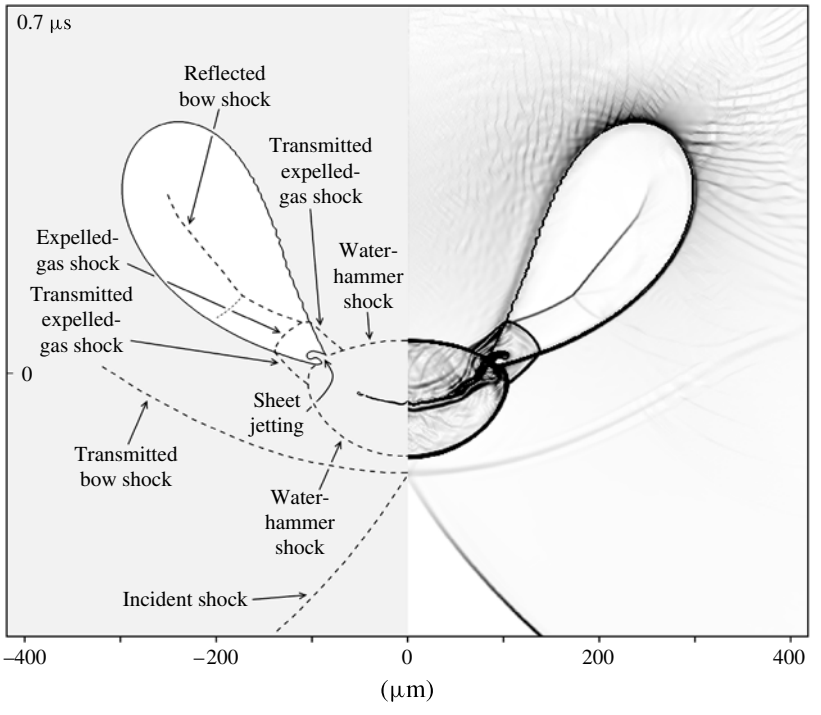


FIGURE 9. Second phase: frame three.

https://doi.org/10.1017/jfm.2012.132 Published online by Cambridge University Press

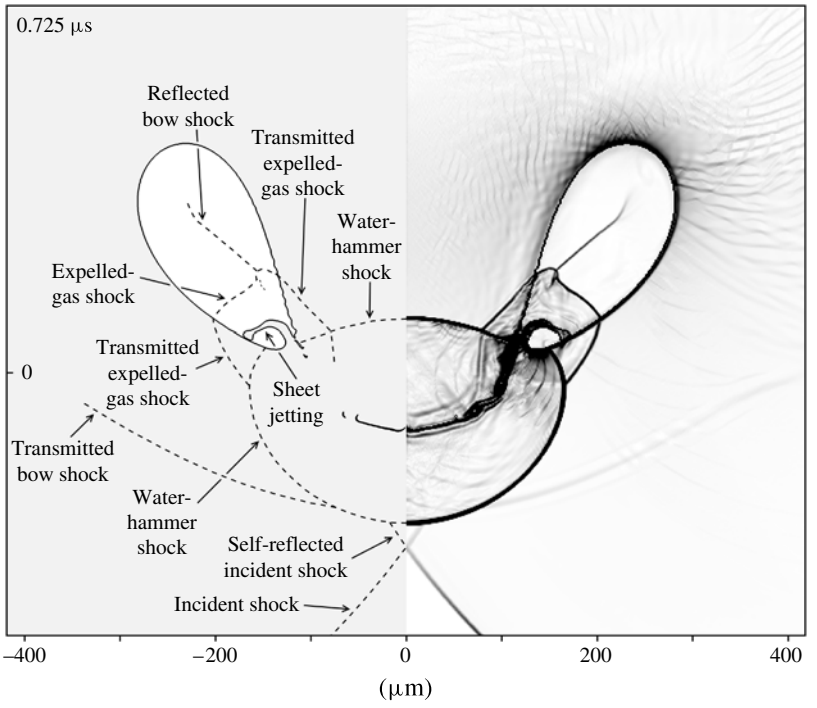


FIGURE 10. Second phase: frame four.

into two parts. As it continues to impact there is a cusp formed corresponding to the position of continuing impact of the side of the main transverse jet and the leeward bubble wall. This violent and continuing collision means that the highest pressures in the water-hammer shock are found at this cusp. It is this region of very high pressure that drives liquid into the gas bubble, forming the sheet jetting. This sheet jetting then moves outwards into the now toroidal bubble at $\sim$3050 m s^{-1}. The Weber number of the sheet jetting is $\sim$3360 (the flow around the jet is travelling at $\sim$2120 m s^{-1}, the density is $\sim$35 kg m^{-3}, the width is $\sim$8 μm and the surface tension coefficient is 0.072). Tong *et al.* (1999) describe a 'splashing' phenomenon that is qualitatively similar to the sheet jetting but is not continuously driven by a region of high pressure in the same way.

Figure 10 (second phase: frame four) shows the formation of another difficult-to-classify transient configuration involving the expelled-gas shock interacting with the remains of the interactions of the bow shock, reflected bow shock and transmitted shock. We can also see here that the distorted incident shock has interacted with itself, forming the self-reflected incident shock. The contact line between the fluid of the main transverse jet and that of the leeward bubble wall can also be seen. The next image, figure 11 (second phase: frame five), shows the time when the contents of the bubble reach their peak temperatures. These occur in two ways: first the sheet-jetting bow shock is very hot ($\sim$24 000 K) and secondly, the sheet jetting greatly compresses the 'tail' of bubble remaining between itself and the main transverse jet, as circled and labelled. The temperatures in this region are $\sim$53 000 K. It is the region containing both of these mechanisms that Bourne & Milne (2003) identifies as the possible cause of the second flash of luminescence, although the specific dynamics are not

https://doi.org/10.1017/jfm.2012.132 Published online by Cambridge University Press

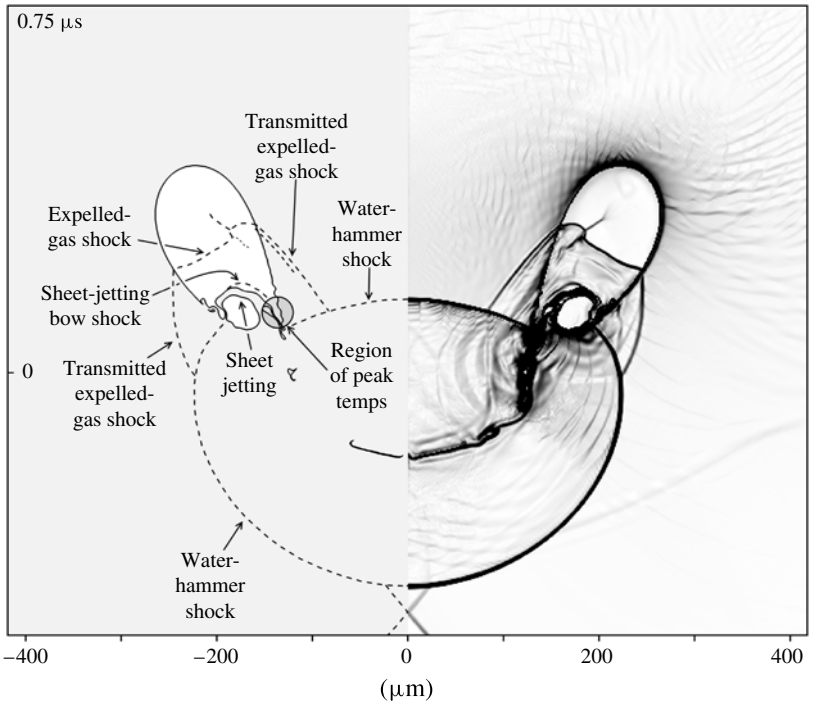


FIGURE 11. Second phase: frame five.

analysed to the level of detail pursued here. Continuing, in figure 12 (second phase: frame six) we see that the shape of the remaining bubble causes the expelled-gas shock to focus on the bubble's most upstream point. As we see in figure 13 (second phase: frame seven), this generates another strong shockwave in the liquid which we call the transmitted focused expelled-gas shock (∼1.4 GPa). Furthermore, additional strong shocks in the liquid are also generated by the impact of the sheet jetting on the bubble wall, as we can see in both figures 13 and 14 (second phase: frame eight), where these are labelled as sheet-jetting shocks (∼2.4 GPa). Ball *et al.* (2000) mentioned the 'compression wave' caused by the focusing of the expelled-gas shock despite not explicitly resolving the shock itself. The sheet-jetting shocks can also be seen in previous work but they have not been discussed (Nourgaliev *et al.* 2006). These newly outlined strong shocks propagate in all directions but their influence is greater on the upstream side of the bubble. By this stage, the numerous interactions of various shockwaves make further analysis of the resulting transient configurations prohibitively complex and possibly of little use. There are also further reflected shocks and shock–contact interactions within the bubble but, as can be seen in the numerical Schlieren plots, these become exceedingly difficult to resolve.

3.1.3. *The third phase: vortex ring*

We define the third phase to start after the water-hammer shock has traversed the remains of the bubble; figure 15 (third phase: frame one) shows the configuration just before this moment. We can see that the sheet-jetting shocks have propagated and interacted with themselves on the axis of symmetry to form reflected sheet-jetting shocks (a representative pressure for these shocks is difficult to determine due to the numerous interactions; however they are around 2.6 GPa). Similarly to the sheet-jetting

https://doi.org/10.1017/jfm.2012.132 Published online by Cambridge University Press

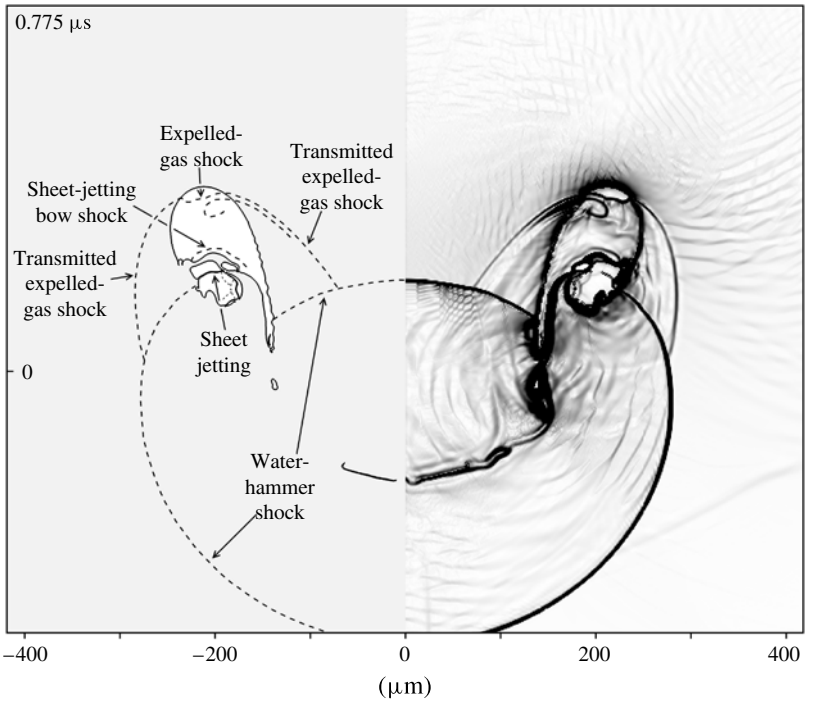


FIGURE 12. Second phase: frame six.

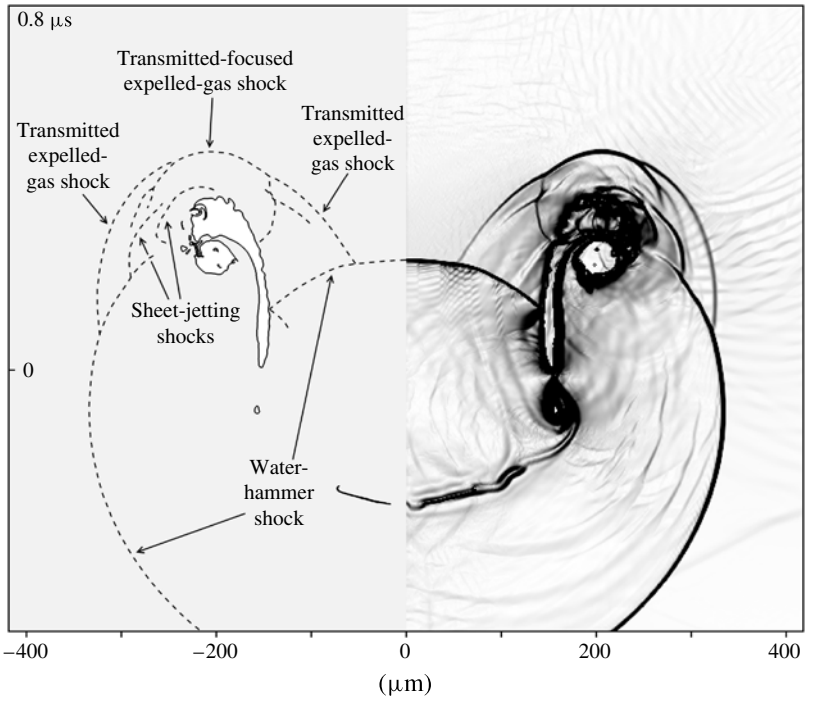


FIGURE 13. Second phase: frame seven.

https://doi.org/10.1017/jfm.2012.132 Published online by Cambridge University Press

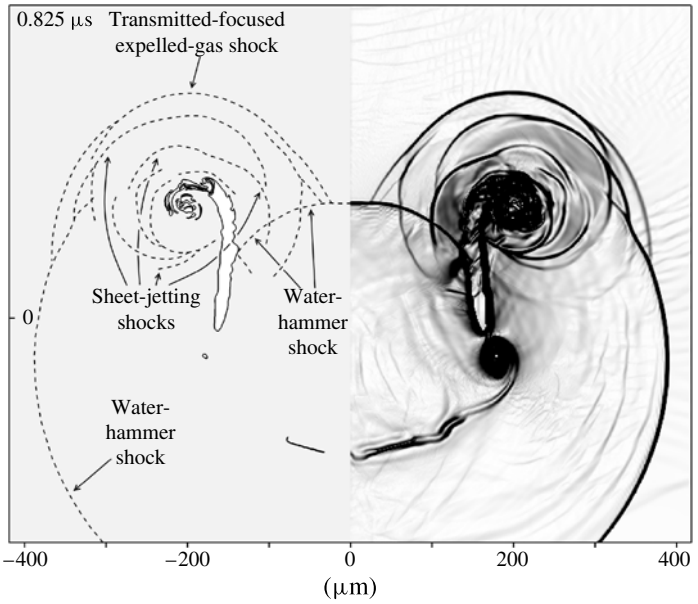


FIGURE 14. Second phase: frame eight.

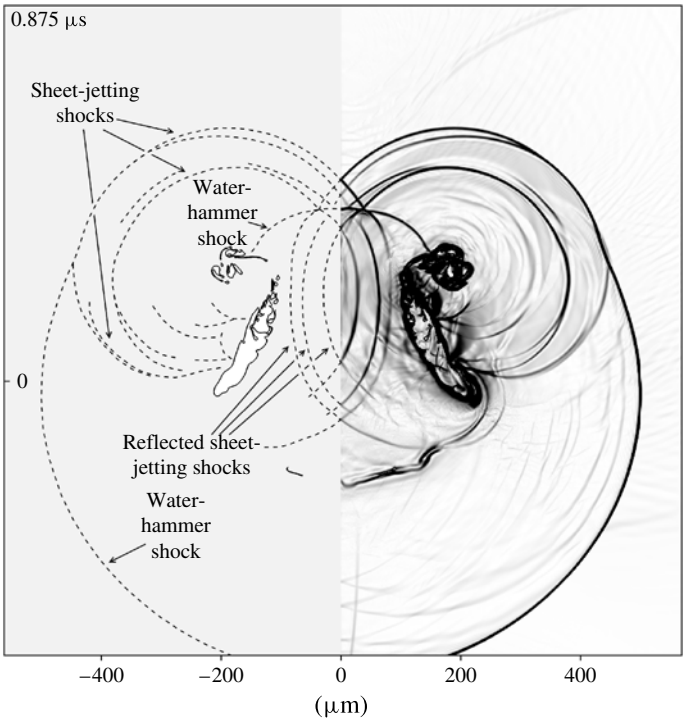


FIGURE 15. Third phase: frame one.

https://doi.org/10.1017/jfm.2012.132 Published online by Cambridge University Press

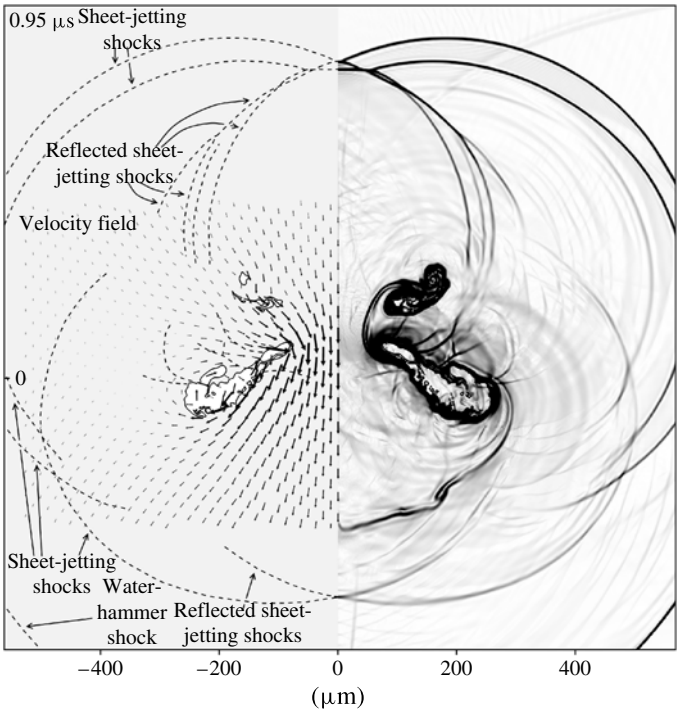


FIGURE 16. Third phase: frame two.

shocks, these propagate in all directions but they are stronger on the upstream side. In fact, the complex interactions of the sheet-jetting shocks, reflected sheet-jetting shocks and water-hammer shock result in the peak pressures observed during the collapse, which are ∼5.5 GPa. It might have been expected that the peak pressures would have occurred at the point of main transverse jet impact but this is not the case. Figure 16 (third phase: frame two) shows the subsequent evolution of these shocks. Now that the violent shockwave interactions have largely finished, the remaining bubble continues to move downwards in the central torus of the vortex ring created by the main transverse jet impact. The velocity field is also shown in figure 16 in order to show the flow field explicitly. The peak velocities at this time are ∼2700 m s^{-1}.

Figure 17 plots the vorticity of the flow at four different times, starting in the second phase (on the left) and moving into the third phase. Vorticity is generated by three mechanisms during the first phase: first by baroclinic generation on the gas–liquid interface, secondly by the various shock–shock interactions and lastly through boundary layer effects. The balance between these mechanisms changes with shock strength, which increases the baroclinic generation, and with bubble size, where the viscous effects become more important at smaller length scales. Vorticity continues to be generated throughout the second phase, as illustrated in the two central frames of figure 17. The culmination of these effects gives rise to the configuration shown in the final frame. Here we can see the large vortex ring close to the bottom, where the bulk of the bubble is contained, and above we can see two smaller secondary vortex rings formed by the sheet jetting.

In the qualitatively similar collapse caused by proximity to a solid wall a counter-jet is observed (Lindau & Lauterborn 2003). This is thought to be caused by an area of

https://doi.org/10.1017/jfm.2012.132 Published online by Cambridge University Press

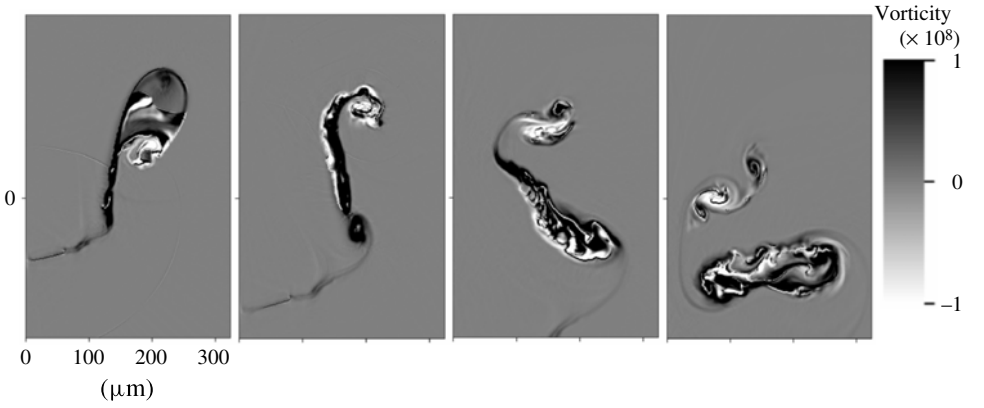


FIGURE 17. Vorticity fields for four time frames; 0.75, 0.825, 0.91 and 1.02 μs after initial contact of shock and bubble, thus in the second and third phases of collapse.

low pressure that is generated on the side opposite the wall and close to the bubble. To our knowledge this phenomenon has not been observed with shock–bubble interaction. We see no hint of an area of low pressure upstream of the bubble; in fact the pressure in this region actually increases due to the stagnation of the oncoming flow (Ding & Gracewski 1996). In our opinion this prevents the formation of a counter-jet. This is the most distinct qualitative difference in the bubble collapse geometry between the two, otherwise similar, mechanisms of non-spherical collapse.

We believe that the sequence of events described above illustrates the mechanisms by which the peak temperatures, and associated luminescence, are reached but we can also draw another interesting conclusion. The water hammer-shock caused by the main transverse jet impact is by no means the only important mechanism as far as cavitation damage is concerned. The transmitted focused expelled-gas shock, sheet-jetting shocks and reflected sheet-jetting shocks are all of significant magnitude and could all affect a nearby surface in the same way the water hammer shock is understood to act. If the incident shock originates from the surface in question (i.e. the surface is upstream) then these additional shocks could exceed the pressure of the water-hammer shock (the water-hammer shock is ∼3 GPa whereas the peak upstream pressures are ∼5.5 GPa). Even in the case where the surface is on the opposite side to the incident shock, the sheet-jetting shocks and reflected sheet-jetting shocks will still have an influence (even after propagating beyond the most downstream point of the bubble the reflected sheet-jetting shocks are still ∼2.1 GPa).

3.2. *Three-dimensional effects: comparing spherical and cylindrical bubbles*

Throughout the paper so far we have analysed planar 2D simulations. However, it is likely that spherical bubbles rather than cylindrical ones will be involved in the various applications we have outlined in § 1, hence here we perform rotationally symmetric and fully 3D simulations. 3D simulations have been performed previously for gas–gas shock–bubble interactions (Niederhaus *et al.* 2008) but, to the best of our knowledge, no such results have ever been presented for a gas bubble in a liquid medium. The aim is to relate our carefully validated cylindrical bubble results to spherical bubbles, thus cross-validating the different models, and also to look for any 3D instability or other differences between full 3D, axisymmetric and 2D results. Fully 3D simulations are inevitably limited in resolution; we use 100 points per radius (p.p.r.), giving 64 000 000

https://doi.org/10.1017/jfm.2012.132 Published online by Cambridge University Press

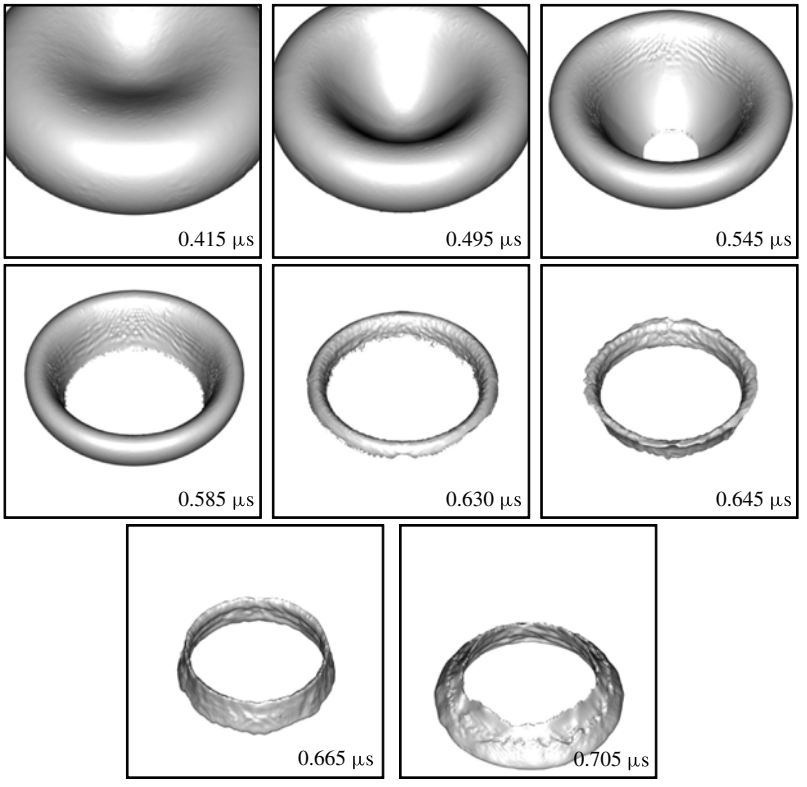


FIGURE 18. Series showing the collapse process simulated in full 3D of a 1 GPa shockwave striking a 1 mm bubble. The bubble stays remarkably rotationally symmetric throughout the collapse. There is a break with rotational symmetry in the fine details of the collapse caused by the impact of the sheet jetting.

cells in total. However, this is enough to qualitatively resolve all the features identified in § 3.1, where the resolution is 400 p.p.r.

Figure 18 shows a time series of a 1 GPa shockwave striking a 1 mm bubble computed in full 3D. This shows no significant deviation from rotational symmetry; the bubble retains an unbroken toroidal shape throughout the second and third phases. The impressive experimental pictures of Lindau & Lauterborn (2003) regarding a bubble collapsing near a wall also display very little in the way of deviation from rotational symmetry. As already mentioned, the collapse geometries are very similar for these two different physical phenomena and hence the lack of 3D effects with collapse near a wall supports our own results. Lindau & Lauterborn (2003) state that initially the bubble surface remains smooth but by the time the collapse moves into the third phase the surface is rough. Our results allow us to explore this.

An important feature observed in the 2D simulations is the sheet jetting and, as we can see in figure 19, this is also manifested in 3D. There is a very clear involution of the bottom of the toroidal bubble caused by the interaction with the water hammer shock, although the constraints on resolution when working in 3D mean that the feature is not as fully resolved as in 2D. The sheet jetting displays a small deviation from rotational symmetry. As it propagates and then interacts with the bubble wall the 3D effects grow. There is an obvious break in the rotational symmetry of the

https://doi.org/10.1017/jfm.2012.132 Published online by Cambridge University Press

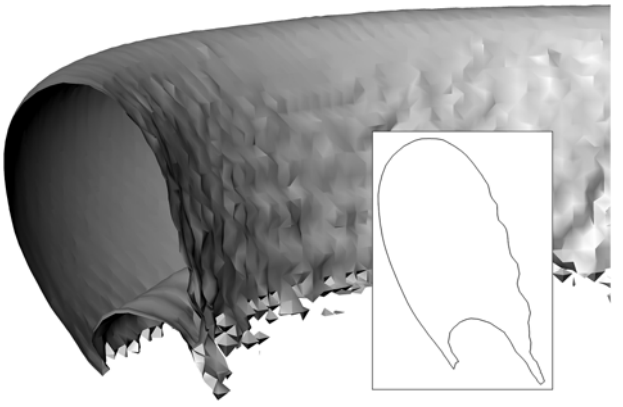


FIGURE 19. Sheet jetting observed in a full 3D simulation. The feature is not as fully resolved as in 2D but there is a very clear involution of the bubble wall driven by the water hammer shock. The inset shows a 2D slice through the 3D results.

	2D	3D	Rotationally symmetric
First phase time (μs)	0.675	0.540	0.540
Second phase time (μs)	0.205	0.175	0.175
Jet speed at impact (m s^{-1})	2278	2754	2737
Water-hammer shock pressure (GPa)	3.00	4.04	4.20

TABLE 1. Comparison of results from 2D, 3D and rotationally symmetric simulations. For a spherical bubble the collapse process is faster and more intense, resulting in a higher water hammer shock pressure.

small-scale details near the end of the second phase, as we can see in figure 18 frame five and six. Taking the 2D and 3D results together it becomes apparent that the roughness described by Lindau & Lauterborn (2003) is caused by the complex interaction of the sheet jetting impacting the bubble wall.

Table 1 compares various quantitative measures between 2D, 3D and rotationally symmetric simulations. It is apparent that the collapse is more intense for a spherical bubble when compared to a cylindrical one; the collapse times are shorter, the main transverse jet speed higher and the water-hammer shock stronger. These effects are expected, due to the higher focusing that the 3D situation entails. In 2D the reflected rarefaction is acting to focus onto a line on top of the initially cylindrical bubble whereas in 3D the focus is a point. This increased degree of focusing gives a faster jet speed. Our simulations show a 21 % increase in the speed of the jet and experimental work indicates an increase of 25 % in the jet speed when comparing cylindrical to spherical bubbles (Bourne & Milne 2003). This increased jet speed causes a stronger water-hammer shock which then yields a faster second-phase collapse time. We estimate the water-hammer shock pressure to be 40 % higher for a spherical bubble. The 3D results are also well supported by the rotationally symmetric runs. The collapse times are the same and the small differences between the other parameters are most likely due to the differing spatial resolutions (the rotationally symmetric run is 400 points per bubble radius whereas the 3D run is 100).

https://doi.org/10.1017/jfm.2012.132 Published online by Cambridge University Press

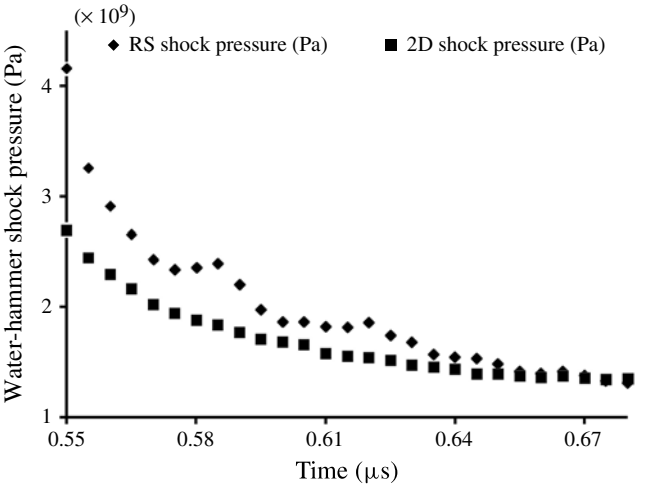


FIGURE 20. Fall-off in water-hammer shock pressure with distance, comparing cylindrical and spherical bubbles. RS denotes rotationally symmetric.

Another difference that we see between spherical and cylindrical bubbles is the fall off of the water-hammer shock pressure as it propagates outwards, as shown in figure 20. This shows a more pronounced fall-off for a spherical bubble. Despite the fact that the water-hammer shock pressure is initially 40 % higher with a spherical bubble, at distance of approximately 0.7 radii away the pressure of the water-hammer shock is actually higher in the cylindrical case.

3.3. *Effects of incident shock pressure*

To study the effects of incident shock pressure we model a 1 mm bubble and use the following incident shock pressures: 100, 200, 500 MPa, 1, 2, 5, 10, 20, 50 and 100 GPa. A parametric study at low shock pressures has been performed by Johnsen & Colonius (2009). Ding & Gracewski (1996) varied both shock strength and bubble size for their study of strong shocks; we aim to provide a more comprehensive study over a much larger range. We have already looked in detail at the collapse process for a 1 GPa incident shock in § 3.1 and we begin by briefly looking at how the dynamics differ for 100 MPa and 100 GPa shockwaves. We then go on to present some quantitative results. 100 GPa is an extremely strong shockwave; however Bourne & Field (1992) discuss creating shocks of 10 GPa within their experimental framework. Hence we felt that 100 GPa was a reasonable upper limit for a parametric study. We find that the incident shock pressure has a much stronger influence on the dynamics than any other factor. The following qualitative discussion applies to both spherical and cylindrical bubbles, but to avoid clutter we shall use terminology from spherical collapse.

3.3.1. *100 MPa incident shock*

A bubble in a liquid subjected to a step change in pressure will begin to collapse in a spherical way. As the shock strength decreases the collapse approaches this idealized case. For a 100 MPa shockwave there is very little immediate effect on the bubble wall; the shock propagates beyond the bubble and the drop in pressure caused by the reflected rarefaction disappears. Thus the bubble finds itself in a high-pressure environment and develops a strong spherical component of collapse. However, the

https://doi.org/10.1017/jfm.2012.132 Published online by Cambridge University Press

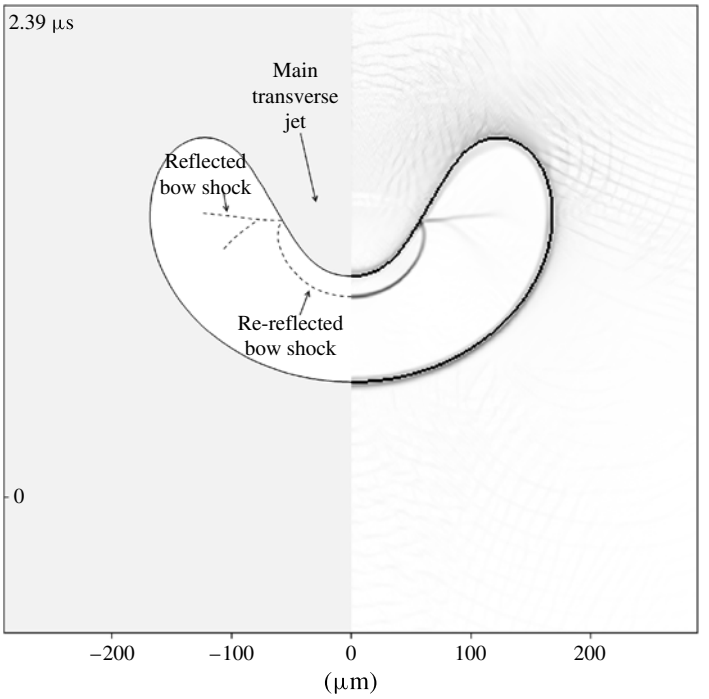


FIGURE 21. 100 MPa: first phase. This, as well as the next two figures, looks at the collapse of a 1 mm bubble by a 100 MPa incident shock. The plots are of the same type as those described in the caption for figure 2.

asphericity of the flow field caused by the reflected rarefaction is still present, i.e. the upstream bubble wall moves inwards faster than the downstream one. As the bubble size decreases the only way that linear momentum can be conserved is through the formation of the main transverse jet. In this way the collapse is very similar to that near a solid wall, referred to in § 1. The slower jet formation can be quantified using the ratio of the first-phase collapse time to that of the second phase and in the 100 MPa case this ratio is ∼28, whereas it was ∼3.3 for the 1 GPa case. Owing to the lower ratio of jet speed to speed of sound in air there is more time for reflections of the bow shock to occur. Figure 21 (100 MPa: first phase) shows the main transverse jet and re-reflected bow shock, which can be seen much more clearly than in the 1 GPa case. There is time for four reflections of the bow shock to occur before jet impact. A consequence of these multiple reflections can be seen with the maximum density of the gas; we return to this in § 3.3.3.

Figure 22 (100 MPa: second phase) shows the situation after the impact of the main transverse jet on the downstream wall; all the familiar features are present. The water-hammer shock is ∼1 GPa, proportionately much higher pressure than for the 1 GPa shock (10:1 compared to 3:1). The expelled-gas shock is also present and due to the multiple reflected shocks within the bubble prior to the jet impact the pressure behind this shock is actually higher than for the 1 GPa shock; it is 0.29 GPa rather than 0.13 GPa. The sheet jetting is still present although it does not emerge until later in the collapse process. When it does emerge it has a lower Weber number of ∼2830, hence it is strongly inertially dominated. However, the 1 GPa incident shock produces sheet jetting with an even higher Weber number and thus there is a

https://doi.org/10.1017/jfm.2012.132 Published online by Cambridge University Press

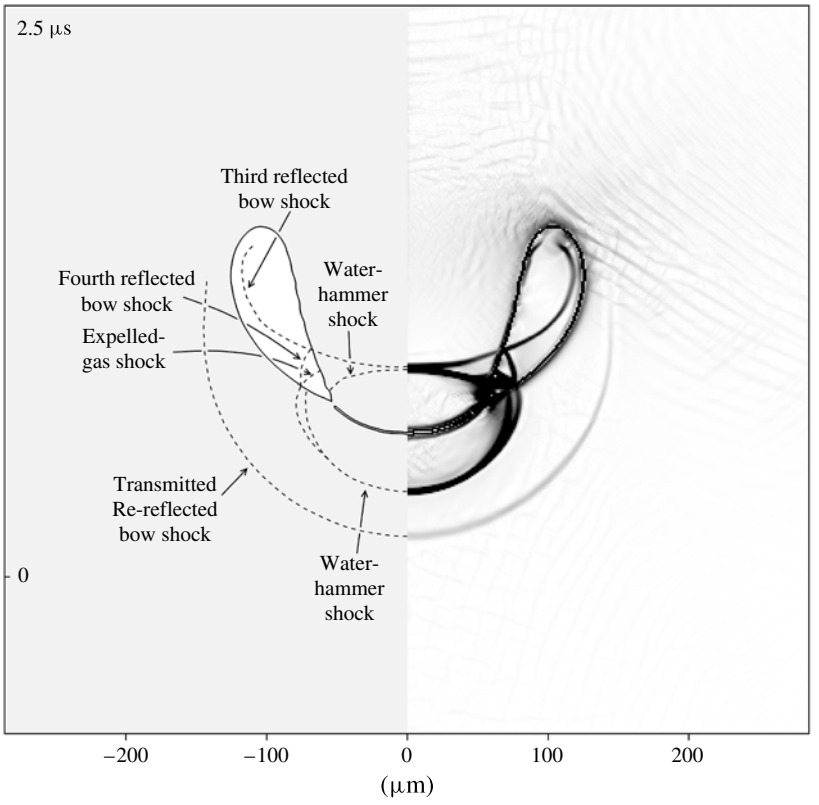


FIGURE 22. 100 MPa: second phase.

correspondingly less complex breakdown in the 100 MPa case. After the impact of the sheet jetting, this leads to a simpler bubble collapse geometry overall. Figure 23 (100 MPa: third phase) shows the third phase and we can see that the shock structures here are considerably simpler than the 1 GPa case. The peak pressures still occur in the interactions of shocks upstream of the bubble and not with the water-hammer shock.

3.3.2. *100 GPa incident shock*

The dynamics for the 100 GPa incident shock are much more complex and violent than the 1 GPa case. As the incident shock interacts with the bubble, the bubble wall reaches Mach 1 relative to the water in ∼60 ps and appears flat with the incident shock. The reflected rarefaction causes the same focusing of flow and the, now familiar, main transverse jet and associated bow shock are formed. Such is the speed of this interaction that the bow shock propagates across the bubble and interacts with the far wall faster than the incident shock can reach it. This can be seen in figure 24 (100 GPa: first phase) where the bow shock has taken a Mach reflection configuration. The flow speed behind a 100 GPa shock is 6075 m s^{-1} and hence we see the development of a water bow shock (∼32 GPa) in the liquid upstream of the bubble. The anomalous reflection configuration reported by Grove & Menikoff (1990) also exhibits increased complexity; the leading edge of the reflected rarefaction has

https://doi.org/10.1017/jfm.2012.132 Published online by Cambridge University Press

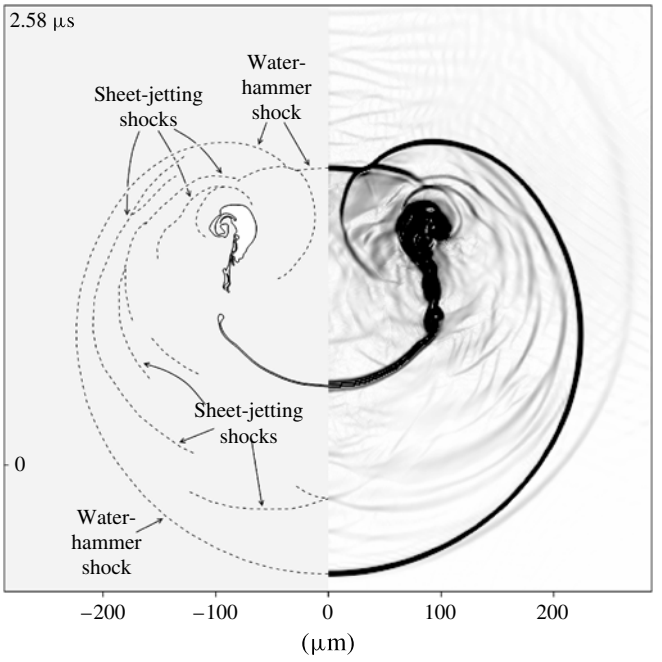


FIGURE 23. 100 MPa: third phase.

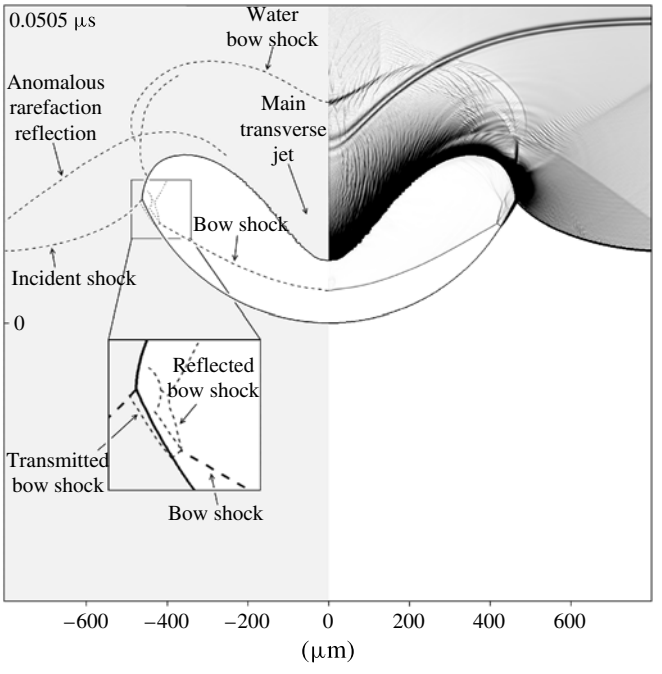


FIGURE 24. 100 GPa: first phase. This, as well as the next two figures, looks at the collapse of a 1 mm bubble by a 100 GPa incident shock. The plots are of the same type as those described in the caption for figure 2.

https://doi.org/10.1017/jfm.2012.132 Published online by Cambridge University Press

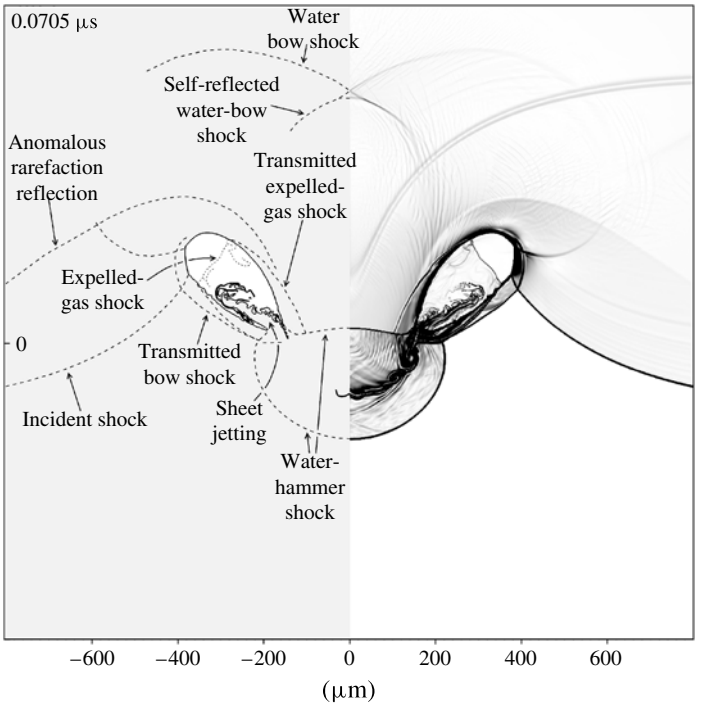


FIGURE 25. 100 GPa: second phase: frame one.

interacted with the incident shock in a manner that appears like reflection. It is unclear to us what the physical significant of this feature is.

Figure 25 (100 GPa: second phase: frame one) shows an image of the second phase of collapse, after the impact of the main transverse jet and formation of the water-hammer shock (∼170 GPa). Again, the familiar features are present. The sheet jetting is very violently thrown outwards into the remaining bubble. It emerges very quickly, travels outwards significantly faster than the water-hammer shock that drives it (∼38 000 m s^{-1}) and the Weber number is ∼188 000. At these Weber numbers the jet breaks down and atomizes extremely rapidly and hence the collapse geometry of the 100 GPa case is much more complex than the previous cases examined. The basic mechanisms by which the peak temperatures were generated in the 1 GPa interaction are still present in the 100 GPa case and seem to indicate a monotonic increase of peak temperature with shock pressure. More sophisticated work regarding the state of extremely compressed gas would be required to confirm this (for example Moss *et al.* 1994). The sheet jetting impacts the far side of the bubble at high speed and, due to the complex geometry, the resulting sheet-jetting shocks are numerous (a representative pressure for these is ∼120 GPa). It becomes difficult to identify the transmitted-focused expelled-gas shock as it is very quickly swamped by the sheet-jetting shocks. The final image, figure 26 (100 GPa: second phase: frame two), shows the complexity of the resulting interactions.

3.3.3. *Quantitative analysis*

When discussing the 100 MPa shock case we mentioned the ratio of the first-phase time to the second-phase time in order to quantify the slower jet formation. Hence figure 27(*a*) presents these times, and figure 27(*b*) the ratio, over our full range

https://doi.org/10.1017/jfm.2012.132 Published online by Cambridge University Press

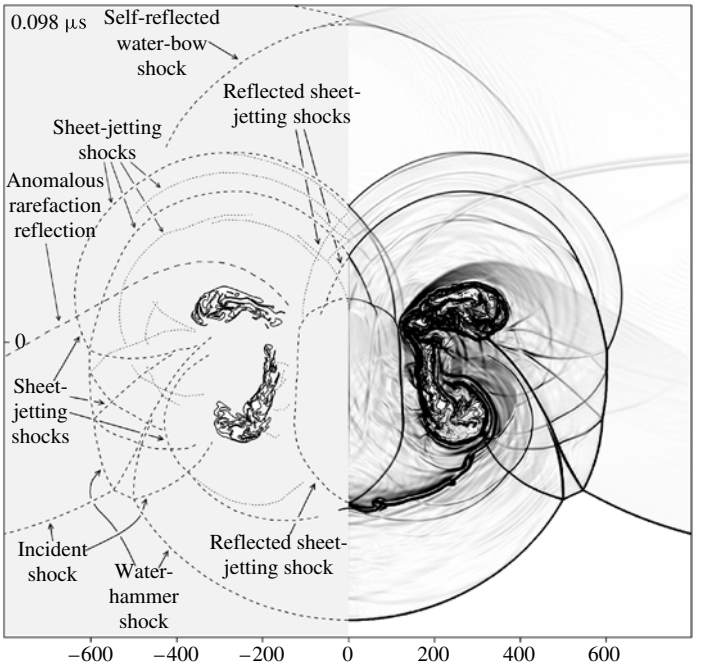


FIGURE 26. 100 GPa: second phase: frame two.

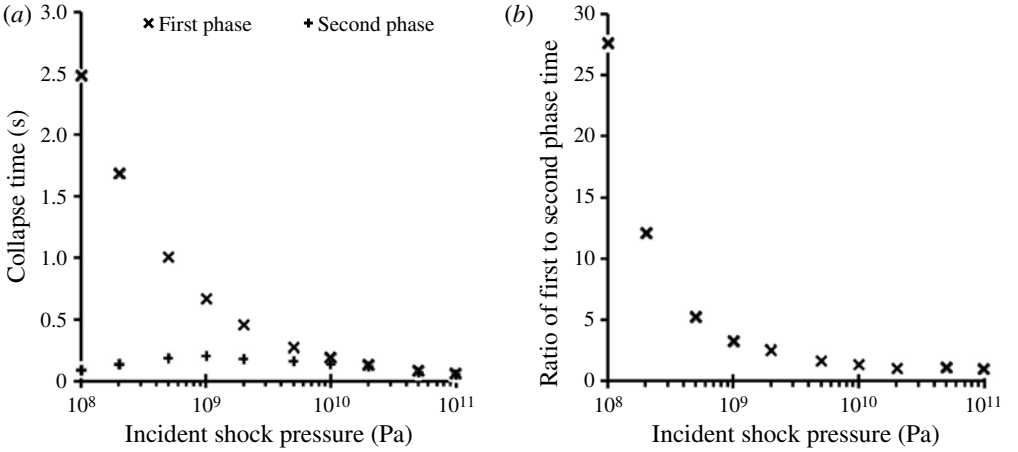


FIGURE 27. (*a*) Variation of the first- and second-phase collapse times over the range of incident shock pressures. The first-phase time shows a clear decreasing trend whereas the second-phase time displays a maximum around 1 GPa. (*b*) Ratio of the first-phase collapse time to the second. This can be used as a measure of the importance of the spherical component of collapse.

of incident shock pressures. The first-phase time shows a clear trend: as the shock pressure is increased the time reduces. Initially the shock has little direct effect on the bubble and it takes time for the imbalance in the flow to manifest and form a jet. The

https://doi.org/10.1017/jfm.2012.132 Published online by Cambridge University Press

collapse dynamics can be thought of as the superposition of a spherical component caused by the step change in pressure and a non-spherical component resulting from the focusing of flow by the reflected rarefaction, yielding the formation of the main transverse jet. At low shock intensities the balance between the two mechanisms can be seen quite plainly. However, as the shock intensity increases the spherical element becomes less important and the shorter first-phase time gives an indication of this change. Eventually the problem is entirely dominated by the non-spherical mechanism and the first-phase time approaches a limit that we can roughly estimate. We know the speed of travel of the incident shockwave and can use this with the bubble size to find the time for the shock to propagate one bubble diameter. For 100 GPa the time to propagate one diameter is 0.061 μs, compared to a collapse time of 0.059 μs in the simulation.

The second-phase time presents a more unusual trend in that it is initially low, rises to a maximum around 1 GPa and then begins to reduce again. We define the second phase to end when the water-hammer shock has finished traversing the toroidal bubble. A higher-pressure shock propagating into the same ahead state will do so faster than a lower-pressure shock. Hence we might expect to see the same trend shown in a curve of the water-hammer shock speed. However, upstream, the water-hammer shock is propagating into the body of the main transverse jet and hence the ahead state is different for each case. Therefore the faster the main transverse jet the stronger the water-hammer shock but also the faster the flow the shock must propagate into becomes (i.e. this velocity is equal to the jet speed). In the frame of reference where the flow ahead of the main transverse jet has zero velocity the shock is moving faster for a higher pressure but in a stationary frame of reference (i.e. the notional laboratory) the water-hammer shock propagates slower. Indeed, the slow upstream propagation of the water-hammer shock has been noted before (Ball *et al.* 2000). Additional factors that affect the second-phase time are the importance of the spherical component of collapse and the sheet jetting. With weaker shocks there is a stronger spherical component of collapse and the first-phase time is also proportionally longer. Hence the average radius of the bubble at the moment of jet impact is less than for a stronger shock, thus affecting the second-phase time. Also, for weaker shocks the sheet jetting lags the water-hammer shock whereas for stronger shocks it leads it. The impact of the sheet jetting thus changes the geometry at the end of the second phase and hence the time at which the water-hammer shock propagates beyond the bubble. Evidently a complex balance of factors yields the shape of the second-phase time curve.

Figure 28 shows how the water-hammer shock pressure, the overall peak pressure and the secondary downstream peak pressure vary with incident shock. A clear trend has been established: when the incident shock pressure is greater than ∼500 MPa the relationship appears to be approximately linear, whereas below this value the pressures are higher than this linear trend. One simple reason for this deviation from linearity could be that the increased time before the formation of the main transverse jet, and hence its impact, allows the downstream wall to reach a non-negligible speed due to the spherical component of the collapse. If this were the case then one would expect the plot of main transverse jet speed with incident shock pressure not to display the deviation from linear shown in the water-hammer shock pressure. However, this is not the case and so the motion of the downstream wall is not the sole reason for the departure from a linear trend.

The results of Johnsen & Colonius (2009) are also shown on figure 28. It can be seen that their values for pressure fit well with ours but that the task of

https://doi.org/10.1017/jfm.2012.132 Published online by Cambridge University Press

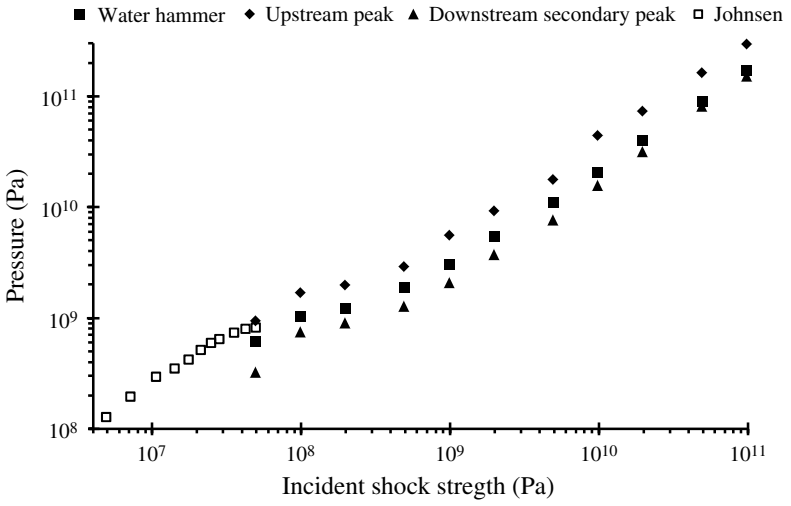


FIGURE 28. Water-hammer shock pressure, peak pressure (which occurs upstream) and the secondary downstream pressure peak plotted against incident shock pressure. Also shown are the results from Johnsen & Colonius (2009).

explaining the trends shown has become more problematic. Their results demonstrate an approximately linear trend at very low shock pressures; then as the shock intensity is increased the pressures start to deviate and are less than the linear trend. For this figure only we have added an additional data point at 50 MPa; a point of inflection can be clearly seen. We speculate that at the lowest shock strengths the spherical component of motion dominates and as the pressure is increased this aspect strengthens. As the non-spherical mechanism becomes more prominent it initially prevents the spherical mechanism from further intensification. However, the non-spherical mechanism may not yet be strong enough to enhance the water-hammer shock. As the non-spherical mechanism begins to strengthen and then dominate the dynamics, the trend then returns to linear. We feel that a full explanation is likely to be more complex; it is clear that a further study that encompasses the entire pressure range could be interesting. It is of course possible that a numerical or modelling reason such as a mismatch of properties of the equation of state could be creating these effects.

Figure 29(*a*) shows the ratio of the water-hammer shock pressure to incident shock pressure. Proportionally the water-hammer shock is strongest at lower shock intensities; it is over 10 times the pressure of the incident shock at 100 MPa. As the intensity rises the ratio tends towards a value of $\sim$1.7. This implies that the water-hammer shock will always be at a higher pressure than the incident shock regardless of how strong the incident shock becomes. The pressure ratio of the water-hammer shock to the peak pressure (upstream) and downstream secondary peak is shown in figure 29(*b*). It can be seen that the relative importance of the different pressures is approximately the same for any incident shock pressure. The secondary downstream peak is $\sim$0.75 times the water-hammer shock pressure, although there may be a slight upward trend beyond 10 GPa. The overall peak pressure is $\sim$1.75 times the water-hammer shock pressure and again a slight upward trend may be present, although the variance is much greater in this case.

https://doi.org/10.1017/jfm.2012.132 Published online by Cambridge University Press

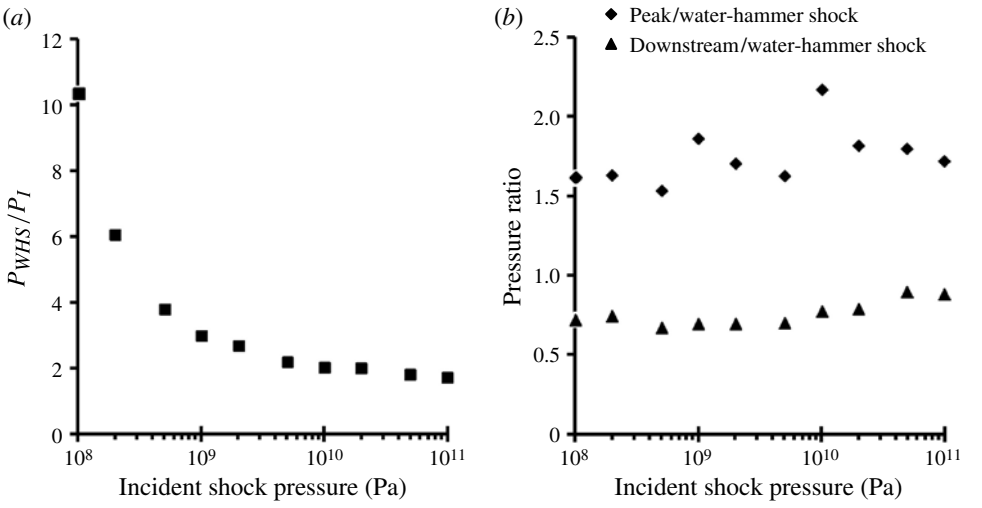


FIGURE 29. (*a*) Ratio of the water-hammer shock pressure to incident shock pressure. Initially this ratio is high and it decreases with increasing pressure, tending towards a value of ∼1.7. (*b*) Ratio of the peak pressure and secondary downstream peak pressure to the water-hammer shock pressure.

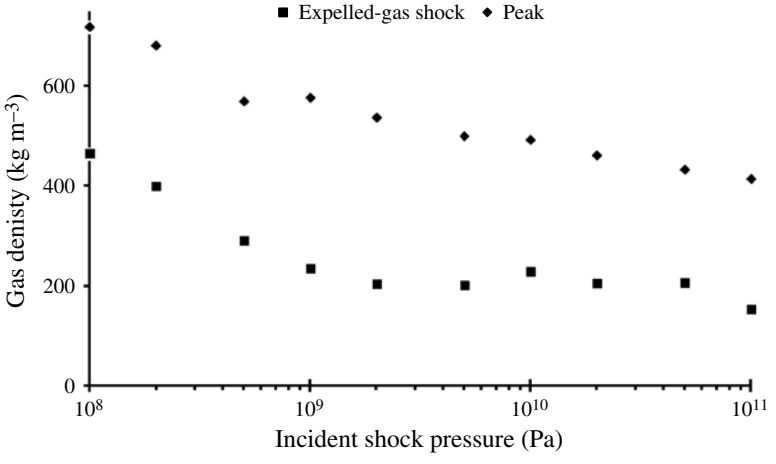


FIGURE 30. Variation of the peak gas density, which occurs under the impacting main transverse jet, and the expelled-gas shock density with incident shock pressure. Surprisingly, the density falls with increasing pressure over the entire range of results.

Figure 30 presents the maximum gas density, which is underneath the tip of the main transverse jet at impact, and the density behind the expelled-gas shock at its formation. Possibly going against intuition, both densities display a downward trend with increasing incident shock pressure. The principal Hugoniot for an ideal gas behaves asymptotically in density, the ratio approaching $(\gamma + 1)/(\gamma - 1)$. As the shock pressure is raised it becomes more and more difficult to increase the density further with a single shock. With multiple shocks one can access a different part of the $p\rho T$ space and it becomes possible to reach higher densities. For the 100 MPa

https://doi.org/10.1017/jfm.2012.132 Published online by Cambridge University Press

collapse we saw that there was time for the bow shock to yield four easily observable reflections. In the 100 GPa case there is only time for one easy-to-see reflection. It is this difference that allows the lower-pressure incident shock to give a higher gas density.

4. Conclusions

We have used a high-accuracy front tracking scheme, *FronTier*, to model a strong shockwave interacting with a gas bubble in a liquid medium. Our methodology has been tested for grid independence and validated against both experimental results and previous numerical work. To begin, we provided a detailed qualitative analysis of the dynamics of the collapse, characterizing it into three phases in each of which a single factor dominates the dynamics (the incident shock, water-hammer shock and vortex ring). By only examining phenomena that we observe across all our simulations we thus develop a language by which these complex processes can be compared and contrasted. Previous work has focused on understanding the first phase and we contributed clarification of the mechanisms at work, such as the formation of the main transverse jet. However, we also comprehensively analysed the later stages of collapse after the jet impact. Within this, we uncovered new dynamics, such as the expelled-gas shock and sheet jetting and their associated consequences, explored the mechanisms by which the peak temperatures and pressures are formed and showed that the water-hammer shock created from the main transverse jet impact is not the only significant high-pressure shock in the liquid.

We performed fully 3D and rotationally symmetric simulations in order to compare spherical and cylindrical bubbles. We observe a lack of any prominent 3D modes in the flow, other than in the small-scale details of the collapse, and conclude that a spherical bubble will produce a water-hammer shock pressure $\sim$40 % higher than a cylindrical one.

We then performed a parametric study over incident shock strength. We identified that the dynamics vary considerably with shock strength and present a qualitative analysis of both 100 MPa and 100 GPa incident shocks. The 100 MPa incident shock has less initial effect on the bubble, which allows the spherical component of collapse caused by a near-instantaneous step in pressure over the shock to take a larger role. The longer collapse time allows more reflections of the bow shock within the bubble. The 100 GPa simulation shows a very high level of complexity; certainly some of the phenomena emerging warrant further exploration. By way of quantitative analysis we showed how the collapse times and the various important pressures, such as the water-hammer shock pressure, vary with incident shock strength. Also, we showed that the relative strengths of these pressures are roughly constant with respect to each other but change in relation to the incident shock pressure. Lastly we showed that, counter-intuitively, the peak gas densities decrease with incident shock pressure due to the reduced time for reflections of the bow shock in the bubble.

Interesting continuations of this work might compare the dynamics of a vapour bubble versus a gas bubble (or a gas bubble with a second vapour phase in it), a distinction shown to be of importance for spherical bubble collapse (Storey & Szeri 2000). A second possibility could be modelling of more complex physical situations, for example a shockwave interacting with multiple bubbles, which has been studied experimentally (Dear & Field 1988), or multiple shockwaves interacting with a single bubble. Within a cloud of transient cavitation bubbles, the bubbles will never be perfectly in phase. It is therefore inevitable that shock–bubble interactions will be taking place and it is very likely that these will be in more complex configurations

https://doi.org/10.1017/jfm.2012.132 Published online by Cambridge University Press

	256 p.p.r.	384 p.p.r.	512 p.p.r.	784 p.p.r.
First phase time (μs)	0.675	0.675	0.675	0.675
Second phase time (μs)	0.205	0.205	0.205	0.205
Main transverse jet velocity at impact (m s^{-1})	2075.6	2078.1	2079.3	2079.9
Water-hammer shock pressure (GPa)	2.90	2.96	2.98	2.99
Sheet jetting velocity (m s^{-1})	3169.8	3345.4	3293	3424.6
Transmitted-focused expelled-gas shock pressure (GPa)	1.46	1.53	1.48	1.55

TABLE 2. Grid independence: the complexity of shock–bubble interaction means that it is easy to reach grid independence in some measures whereas others are more difficult.

than studied here. Detailed simulations of these cooperative effects would be an interesting challenge. Lastly, examining the conditions of luminescence in a more robust way through superior equation-of-state modelling would also be a worthwhile new direction.

Acknowledgements

The authors would like to acknowledge the support of the Engineering and Physical Sciences Research Council, through grant EP/F033710/1 and also through an EPSRC doctoral studentship. The authors would like to acknowledge the use of Frontier and helpful discussions with Professor X. Li of Stony Brook University.

Supplementary movie files available at journals.cambridge.org/flm.

Appendix

In this appendix we check the model for self-consistency and provide validation. First, we conduct a detailed grid-independence analysis and secondly, we compare our results to the scarce experimental evidence involving strong shockwaves, as well as with previous numerical work.

A.1. *Grid independence*

The complexity of shock–bubble interaction makes complete grid independence, in the strictest sense, difficult to achieve. However, all the dynamics qualitatively identified and categorized have been well resolved. For some features, such as the main transverse jet and the first-phase collapse time, full grid independence can be achieved on a desktop computer. However other behaviour is less easy to resolve. No matter what the resolution, the impact of the main transverse jet on the leeward bubble wall will always be a point event. The sheet jetting, which results directly from this point event, is the most difficult phenomenon to resolve. The precise geometry of breakdown continues to increase in complexity with resolution beyond what we can achieve. However, the speed, the thermodynamic states of the sheet jetting and of its surroundings (i.e. the sheet-jetting bow shock) and the envelope region traced out by its motion are all well resolved. This is demonstrated quantitatively in table 2. Having explored resolutions ranging from 50 to 784 points per initial bubble radius (p.p.r.) and having analysed and compared the results obtained, we have progressed with a spatial resolution of 400 p.p.r. At this point we note that a simulation at this resolution takes roughly 3 days when computed on 162.66 GHz cores.

https://doi.org/10.1017/jfm.2012.132 Published online by Cambridge University Press

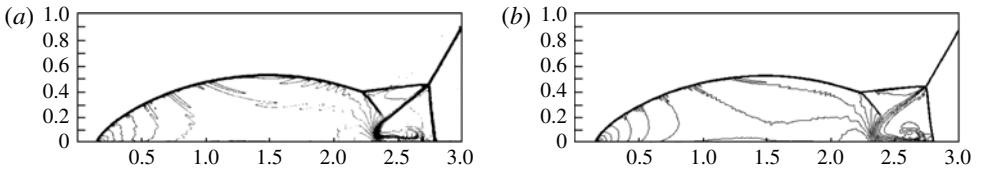


FIGURE 31. Comparing shockwave structure for a double Mach reflection: (*a*) present work (FronTier's MUSCL solver); (*b*) results from the study by Woodward & Colella (1984).

	Bourne & Field (1992) (experimental)	Ball *et al.* (2000)	Nourgaliev *et al.* (2006)	Present work
Collapse time (μs)	1.8 ± 0.2	3.1	3.69	2.8
Jet velocity at impact (m s^{-1})	3300 ± 300	2600	2850	2810
Peak pressure on jet impact (GPa)	N/A	4.7	10.1	5.89

TABLE 3. Validation through comparison to both experiment and previous modelling. There is discrepancy between the modelling work and experiment, partly attributed to the gel medium used for the experiment versus the modelled water.

A.2. *Validation*

Our first validation step aimed to check the ability of *FronTier*'s MUSCL implementation to accurately capture complex shockwave configurations. To do this we drew on the very well-known paper by Woodward & Colella (1984). Figure 31(*a*) shows our results and those for comparison in figure 31(*b*); it can be seen that there is an excellent agreement.

To validate the shock–bubble interaction simulations, we draw comparison to the experimental work of Bourne & Field (1992). This looks at a shockwave collapsing a cylindrical bubble between two glass sheets and hence, as mentioned in § 2.3, we model the problem in plane 2D. This experimental data set of a 1.9 GPa shockwave striking a 6 mm bubble has been used by other authors for validation (Ball *et al.* 2000; Nourgaliev *et al.* 2006; Chang & Liou 2007); therefore we shall use this to allow comparison to other numerical work at the same time. Table 3 presents this comparison. Our work fits in well with both the experimental evidence and the numerical modelling, although there are discrepancies between all sources of data. Bourne & Field (1992) used a 12 % mixture of gelatine and water that allowed the bubbles to be prefabricated and fixed within the resulting semi-solid jelly. They state that this material loses its viscoelastic properties upon being shocked, behaving like pure water. This is undoubtedly not perfectly the case. All the numerical results here model pure water and we believe this is likely to explain, at least partly, the difference in jet speed and collapse time when compared with the experimental evidence. The discrepancy in the pressures between the numerical results is likely to come from the nature of the measurement itself, as well as the differing equations of state. This is the peak pressure at the impact of the main transverse jet, which occurs after the initial impact at the cusp formed between the jet and the leeward wall. Precise spatial resolution of this singularity is very difficult to achieve and, compounding the problem,

https://doi.org/10.1017/jfm.2012.132 Published online by Cambridge University Press

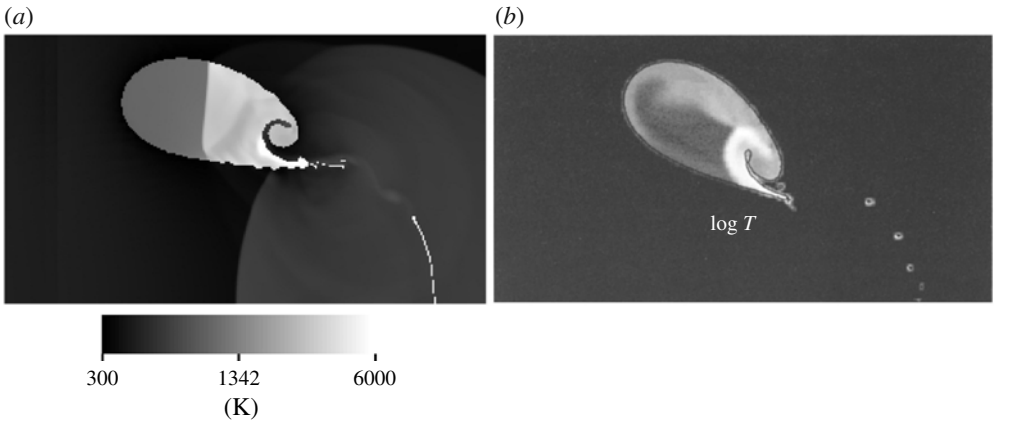


FIGURE 32. Temperature plots illustrating the region of the second flash of luminescence: (*a*) our results; (*b*) results from the study by (Bourne & Milne 2003). The peak temperature in Bourne's work is ∼6000 K whereas here is it ∼14 000 K.

the peak pressure observed would also be highly dependent on the temporal resolution of the output. A better way to measure the water-hammer shock pressure would be to use an averaged representative value from a few moments after impact, as is done elsewhere in this paper. Were it possible to compare the representative value with previous work we believe the pressures would be less widely spread.

In addition to the above comparisons we present a temperature plot to be qualitatively compared to the modelling of Bourne & Milne (2003). Figure 32(*a*) shows our results and figure 32(*b*) shows results from Bourne & Milne (2003). As previously mentioned this work used a sophisticated equation of state to examine the temperatures within a shock-collapsed bubble. They aimed to understand the two flashes of luminescence that they had observed experimentally (Bourne & Field 1999). As discussed, we use the ideal-gas equation of state and hence we cannot predict quantitatively accurate temperatures. However, it can be seen that we still observe a qualitative similar temperature distribution. Hence our ideal-gas model still captures the hydrodynamics mechanisms that lead to the flashes of luminescence. We can also get an indication of the errors of modelling ideal gas; our peak temperature is ∼14 000 K whereas theirs is ∼6000 K (Bourne & Milne 2003).

REFERENCES

ARORA, M., JUNGE, L. & OHL, C. D. 2005 Cavitation cluster dynamics in shock-wave lithotripsy. Part 1. Free field. *Ultrasound Med. Biol.* **31** (6), 827–839.

BALL, G. J., HOWELL, B. P., LEIGHTON, T. G. & SCHOFIELD, M. J. 2000 Shock-induced collapse of a cylindrical air cavity in water: a free-Lagrange simulation. *Shock Waves* **10** (4), 265–276.

BARBER, B. P., HILLER, R. A., LOFSTEDT, R., PUTTERMAN, S. J. & WENINGER, K. R. 1997 Defining the unknowns of sonoluminescence. *Phys. Rep.* **281** (2), 65–143.

BENJAMIN, T. B. & ELLIS, A. T. 1966 The collapse of cavitation bubbles and the pressures thereby produced against solid boundaries. *Phil. Trans. R. Soc. Lond.* A **260** (1110), 221–240.

BJERKNES, V. F. K. 1906 *Fields of Force*. Columbia University Press.

BOURNE, N. K. 2002 On the collapse of cavities. *Shock Waves* **11** (6), 447–455.

https://doi.org/10.1017/jfm.2012.132 Published online by Cambridge University Press

BOURNE, N. K. & FIELD, J. E. 1992 Shock-induced collapse of single cavities in liquids. *J. Fluid Mech.* **244**, 225–240.

BOURNE, N. K. & FIELD, J. E. 1999 Shock-induced collapse and luminescence by cavities. *Phil. Trans. R. Soc. Lond.* A **357**, 295–311.

BOURNE, N. K. & MILNE, A. M. 2003 The temperature of a shock-collapsed cavity. *Proc. R. Soc. Lond.* A **459** (2036), 1851–1861.

BOWDEN, F. & GURTON, O. 1948 Birth and growth of the explosion in solids initiated by impact. *Nature* **161**, 348.

BRACKBIL, J., KOTHE, D. & ZEMACH, C. 1992 A continuum method for modeling surface tension. *J. Comput. Phys.* **100**, 335–354.

BRENNER, M., HILGENFELDT, S. & LOHSE, D. 2002 Single-bubble sonoluminescence. *Rev. Mod. Phys.* **74** (2), 425–484.

BRUJAN, E. A., KEEN, G. S., VOGEL, A. & BLAKE, J. R. 2002 The final stage of the collapse of a cavitation bubble close to a rigid boundary. *Phys. Fluids* **14** (1), 85–92.

CHANG, C.-H. & LIOU, M.-S. 2007 A robust and accurate approach to computing compressible multiphase flow: stratified flow model and AUSM+-up scheme. *J. Comput. Phys.* **225** (1), 840–873.

COLELLA, P. 1985 A direct Eulerian MUSCL scheme for gas dynamics. *SIAM J. Sci. Stat. Comput.* **6** (1), 104–117.

COLEY, G. D. & FIELD, J. E. 1973 The role of cavities in the initiation and growth of explosion in liquids. *Proc. R. Soc. Lond.* A **335** (1600), 67–86.

COOK, S. S. 1928 Erosion by water-hammer. *Proc. R. Soc. Lond.* A **119** (783), 481–488.

COURANT, R., FRIEDRICHS, K. & LEWY, H. 1967 On the partial difference equations of mathematical physics. *IBM J. Res. Dev.* **11** (2), 215–234.

DEAR, J. & FIELD, J. E. 1988 A study of the collapse of arrays of cavities. *J. Fluid Mech.* **190**, 409–425.

DIDENKO, Y. T. & GORDEYCHUK, T. 2000 Multibubble sonoluminescence spectra of water which resemble single-bubble sonoluminescence. *Phys. Rev. Lett.* **84** (24), 5640–5643.

DING, Z. & GRACEWSKI, S. M. 1996 The behaviour of a gas cavity impacted by a weak or strong shock wave. *J. Fluid Mech.* **309**, 183–209.

DU, J., FIX, B., GLIMM, J., JIA, X., LI, X., LI, Y. & WU, L. 2006 A simple package for front tracking. *J. Comput. Phys.* **213** (2), 613–628.

FIX, B., GLIMM, J., KAUFMAN, R., LI, X. & WU, L. 2008 Verification and validation of FronTier code and application to fluid interfacial instabilities. *Phys. Scr.* **T132**, 1–6.

FLANNIGAN, D. J. & SUSLICK, K. S. 2005 Plasma formation and temperature measurement during single-bubble cavitation. *Nature* **434**, 52–55.

FRENZEL, H. & SCHULTES, H. 1934 Luminescenz im ultraschallbeschickten Wasser. *Z. Phys. Chem.* **27b**, 421.

GAITAN, D. F., CRUM, L. A., CHURCH, C. C. & ROY, R. A. 1992 Sonoluminescence and bubble dynamics for a single, stable, cavitation bubble. *J. Acoust. Soc. Am.* **91** (6), 3166–3183.

GILMORE, F. R. 1952. The growth or collapse of a spherical bubble in a viscous compressible liquid. *Hydrodynamics Lab. Rep.* 26-4. California Institute of Technology.

GLIMM, J. 1988 The interaction of nonlinear hyperbolic waves. *Commun. Pure Appl. Maths* **41** (5), 569–590.

GLIMM, J. 1998 Front tracking in two and three dimensions. *Comput. Maths Applics.* **35** (7), 1–11.

GLIMM, J., GROVE, J. W., LI, X., SHYUE, K.-M., ZENG, Y. & ZHANG, Q. 1998 Three-dimensional front tracking. *SIAM J. Sci. Comput.* **19** (3), 703–723.

GLIMM, J., GROVE, J. W., LI, X. & TAN, D. C. 2000 Robust computational algorithms for dynamic interface tracking in three dimensions. *SIAM J. Sci. Comput.* **21** (6), 2240–2256.

GLIMM, J., GROVE, J. W., LI, X. & ZHAO, N. 1999 Simple front tracking. *Contemp. Maths* **238**, 133–149.

GLIMM, J., GROVE, J. W., LINDQUIST, B., MCBRYAN, O. A. & TRYGGVASON, G. 1988 The bifurcation of tracked scalar waves. *SIAM J. Sci. Stat. Comput.* **9** (1), 61–79.

GLIMM, J., GROVE, J. W. & ZHANG, Y. 2002 Interface tracking for axisymmetric flows. *SIAM J. Sci. Comput.* **24** (1), 208–236.

https://doi.org/10.1017/jfm.2012.132 Published online by Cambridge University Press

GLIMM, J., ISAACSON, E., MARCHESIN, D. & MCBRYAN, O. A. 1981 Front tracking for hyperbolic systems. *Adv. Appl. Maths* **2**, 91–119.

GLIMM, J., LI, X., LIU, Y., XU, Z. & ZHAO, N. 2003 Conservative front tracking with improved accuracy. *SIAM J. Numer. Anal.* **41** (5), 1926–1947.

GLIMM, J. & MCBRYAN, O. A. 1985 A computational model for interfaces. *Adv. Appl. Maths* **6**, 422–435.

GLIMM, J., MCBRYAN, O. A., MENIKOFF, R. & SHARP, D. H. 1986 Front tracking applied to Rayleigh–Taylor instability. *SIAM J. Sci. Stat. Comput.* **7** (1), 230–251.

GROVE, J. W. 1994 Applications of front tracking to the simulation of shock refractions and unstable mixing. *Appl. Numer. Maths* **14** (1–3), 213–237.

GROVE, J. W. & MENIKOFF, R. 1990 Anomalous reflection of a shock wave at a fluid interface. *J. Fluid Mech.* **219**, 313–336.

HAAS, J. F. & STURTEVANT, B. 1987 Interaction of weak shock waves with cylindrical and spherical gas inhomogeneities. *J. Fluid Mech.* **181**, 41–76.

HALLER, K. K., POULIKAKOS, D., VENTIKOS, Y. & MONKEWITS, P. 2003 Shock wave formation in droplet impact on a rigid surface: lateral liquid motion and multiple wave structure in the contact line region. *J. Fluid Mech.* **490**, 1–14.

HALLER, K. K., VENTIKOS, Y. & POULIKAKOS, D. 2003 Wave structure in the contact line region during high speed droplet impact on a surface: solution of the Riemann problem for the stiffened gas equation of state. *J. Appl. Phys.* **93** (5), 3090–3097.

HALLER, K. K., VENTIKOS, Y., POULIKAKOS, D. & MONKEWITZ, P. 2002 Computational study of high-speed liquid droplet impact. *J. Appl. Phys.* **92** (5), 2821–2828.

HANSSON, I., KEDRINSKII, V. & MORCH, K. A. 1982 On the dynamics of cavity clusters. *J. Phys.* D: *Appl. Phys.* **15** (9), 1725–1734.

HARLOW, F. H. & WELCH, J. E. 1965 Numerical calculation of time-dependent viscous incompressible flow of fluid with free surface. *Phys. Fluids* **8** (12), 2182–2189.

HILLER, R. A., PUTTERMAN, S. J. & BARBER, B. P. 1992 Spectrum of synchronous picosecond sonoluminescence. *Phys. Rev. Lett.* **69** (8), 1182–1184.

HIRT, C. & NICHOLS, B. 1981 Volume of fluid (VOF) method for the dynamics of free boundaries. *J. Comput. Phys.* **39** (1), 201–225.

JIAO, X. & ZHA, H. 2008 Consistent computation of first- and second-order differential quantities for surface meshes. In *Proceedings of the 2008 ACM Symposium on Solid and Physical Modelling*. pp. 159–170. ACM.

JOHNSEN, E. & COLONIUS, T. 2006 Implementation of WENO schemes in compressible multicomponent flow problems. *J. Comput. Phys.* **219** (2), 715–732.

JOHNSEN, E. & COLONIUS, T. 2008 Shock-induced collapse of a gas bubble in shockwave lithotripsy. *J. Acoust. Soc. Am.* **124** (4), 2011–2020.

JOHNSEN, E. & COLONIUS, T. 2009 Numerical simulations of non-spherical bubble collapse. *J. Fluid Mech.* **629**, 231–262.

KELLER, J. B. & MIKSIS, M. 1980 Bubble oscillations of large amplitude. *J. Acoust. Soc. Am.* **68** (2), 628–633.

KLASEBOER, E., FONG, S. W., TURANGAN, C. K., KHOO, B. C., SZERI, A. J., CALVISI, M. L. & SANKIN, G. N. *et al*. 2007 Interaction of lithotripter shockwaves with single inertial cavitation bubbles. *J. Fluid Mech.* **593**, 33–56.

KODAMA, T. & TOMITA, Y. 2000 Cavitation bubble behaviour and bubble-shock wave interaction near a gelatin surface as a study of in vivo bubble dynamics. *Appl. Phys.* B **70** (1), 139–149.

KORNFELD, M. & SUVOROV, L. 1944 On the destructive action of cavitation. *J. Appl. Phys.* **15**, 495–506.

KRÖNINGER, D., KÖHLER, K., KURZ, T. & LAUTERBORN, W. 2010 Particle tracking velocimetry of the flow field around a collapsing cavitation bubble. *Exp. Fluids* **48** (3), 395–408.

LAUTERBORN, W. & BOLLE, H. 1975 Experimental investigations of cavitation-bubble collapse in the neighbourhood of a solid boundary. *J. Fluid Mech.* **72** (02), 391–399.

LAUTERBORN, W. & KURZ, T. 2010 Physics of bubble oscillations. *Rep. Prog. Phys.* **73** (10) 1–88.

https://doi.org/10.1017/jfm.2012.132 Published online by Cambridge University Press

LEIGHTON, T. G., FEDELE, F., COLEMAN, A., MCCARTHY, C., RYVES, S., HURRELL, A. M. & DE STEFANO, A. *et al.* 2008. Clinical studies of real-time monitoring of lithotripter performance using passive acoustic ensors. *2nd International Urolithiasis Research Symposium*, pp. 256-277. AIP.

LI, X. 1996 Numerical study for the three-dimensional Rayleigh–Taylor Instability through the TVD/AC scheme and parallel computation. *J. Comput. Phys.* **126** (2), 343–355.

LINDAU, O. & LAUTERBORN, W. 2003 Cinematographic observation of the collapse and rebound of a laser-produced cavitation bubble near a wall. *J. Fluid Mech.* **479**, 327–348.

LIU, X., LI, Y., GLIMM, J. & LI, X. 2007 A front tracking algorithm for limited mass diffusion. *J. Comput. Phys.* **222** (2), 644–653.

LU, T., XU, Z., SAMULYAK, R., GLIMM, J. & JI, X. M. 2008 Dynamics phase boundaries for compressible fluids. *SIAM J. Sci. Comput.* **30** (2), 895–915.

MADER, C. L. 1965 Initiation of detonation by the interaction of shocks with density discontinuities. *Phys. Fluids* **8** (10), 1811–1816.

MATULA, T. & CRUM, L. A. 1998 Evidence for gas exchange in single-bubble sonoluminescence. *Phys. Rev. Lett.* **80** (4), 865–868.

MCNAMARA, W. B., DIDENKO, Y. T. & SUSLICK, K. S. 1999 Sonoluminescence temperatures during multi-bubble cavitation. *Nature* **401** (6755), 772–775.

MELLEN, R. H. 1956 An experimental study of the collapse of a spherical cavity in water. *J. Acoust. Soc. Am.* **28** (3), 447–454.

MENIKOFF, R. & PLOHR, B. J. 1989 The Riemann problem for fluid flows of real materials. *Rev. Mod. Phys.* **61** (1), 75–130.

MOSS, W. C., CLARKE, D. B., WHITE, J. W. & YOUNG, D. A. 1994 Hydrodynamic simulations of bubble collapse and picosecond sonoluminescence. *Phys. Fluids* **6** (9), 2979–2985.

NAGAYAMA, K., MORI, Y., SHIMADA, K. & NAKAHARA, M. 2002 Shock Hugoniot compression curve for water up to 1 GPa by using a compressed gas gun. *J. Appl. Phys.* **91** (1), 476–482.

NIEDERHAUS, J. H. J., GREENOUGH, J. A., OAKLEY, J. G., RANJAN, D., ANDERSON, M. H. & BONAZZA, R. 2008 A computational parameter study for the three-dimensional shock–bubble interaction. *J. Fluid Mech.* **594**, 85–124.

NIGMATULIN, R. I., AKHATOV, I. S., TOPOLNIKOV, A. S., BOLOTNOVA, R. K., VAKHITOVA, N. K., LAHEY, R. T. JR. & TALEYARKHAN, R. P. 2005 Theory of supercompression of vapor bubbles and nanoscale thermonuclear fusion. *Phys. Fluids* **17** (10), 107106.

NOURGALIEV, R. R., DINH, T. N. & THEOFANOUS, T. G. 2006 Adaptive characteristics-based matching for compressible multifluid dynamics. *J. Comput. Phys.* **213** (2), 500–529.

PELEKASIS, N. A. & TSAMOPOULOS, J. A. 1993*a* Bjerknes forces between two bubbles. Part 1. Response to a step change in pressure. *J. Fluid Mech.* **254**, 467–499.

PELEKASIS, N. A. & TSAMOPOULOS, J. A. 1993*b* Bjerknes forces between two bubbles. Part 2. Response to an oscillatory pressure field. *J. Fluid Mech.* **254**, 501–527.

PHILIPP, A. & LAUTERBORN, W. 1998 Cavitation erosion by single laser-produced bubbles. *J. Fluid Mech.* **361**, 75–116.

PLESSET, M. S. 1949 The dynamics of cavitation bubbles. *Trans. ASME: J. Appl. Mech.* **16** (3), 227–282.

PLESSET, M. S. & CHAPMAN, R. B. 1971 Collapse of an initially spherical vapour cavity in the neighbourhood of a solid boundary. *J. Fluid Mech.* **47** (2), 283–290.

PLESSET, M. S. & PROSPERETTI, A. 1977 Bubble dynamics and cavitation. *Annu. Rev. Fluid Mech.* **9** (1), 145–185.

PROSPERETTI, A. 1997 A new mechanism for sonoluminescence. *J. Acoust. Soc. Am.* **101** (4), 2003–2007.

QUIRK, J. J. & KARNI, S. 1996 On the dynamics of a shock–bubble interaction. *J. Fluid Mech.* **318**, 129–163.

RANJAN, D., NIEDERHAUS, J. H. J., OAKLEY, J. G., ANDERSON, M. H., BONAZZA, R. & GREENOUGH, J. A. 2008 Shock-bubble interactions: features of divergent shock-refraction geometry observed in experiments and simulations. *Phys. Fluids* **20** (3), 036101.

https://doi.org/10.1017/jfm.2012.132 Published online by Cambridge University Press

RAY, J., SAMTANEY, R. & ZABUSKY, N. J. 2000 Shock interactions with heavy gaseous elliptic cylinders: two leeward-side shock competition modes and a heuristic model for interfacial circulation deposition at early times. *Phys. Fluids* **12** (3), 707–716.

RAYLEIGH, LORD 1917 On the pressure developed in a liquid during the collapse of a spherical cavity. *Phil. Mag.* **34**, 94–98.

SAMTANEY, R., RAY, J. & ZABUSKY, N. J. 1998 Baroclinic circulation generation on shock accelerated slow/fast gas interfaces. *Phys. Fluids* **10** (5), 1217–1230.

SETHIAN, J. A. 1999 *Level Set Methods and Fast Marching Methods*. Cambridge University Press.

SHAPIRA, D. & SALTMARSH, M. 2002 Nuclear fusion in collapsing bubbles – Is it there? An attempt to repeat the observation of nuclear emissions from sonoluminescence. *Phys. Rev. Lett.* **89** (10), 2–5.

STOREY, B. D. & SZERI, A. J. 2000 Water vapour, sonoluminescence and sonochemistry. *Proc. R. Soc. Lond.* A **456**, 1685–1709.

SUSLICK, K. S. 1990 Sonochemistry. *Science* **247** (4949), 1439–1445.

SUSLICK, K. S., DOKTYCZ, S. & FLINT, E. 1990 On the origin of sonoluminescence and sonochemistry. *Ultrasonics* **28** (5), 280–290.

SUSLICK, K. S. & FLANNIGAN, D. J. 2008 Inside a collapsing bubble: sonoluminescence and the conditions during cavitation. *Annu. Rev. Phys. Chem.* **59**, 659–683.

TAKAHIRA, H., MATSUNO, T. & SHUTO, K. 2008 Numerical investigations of shock–bubble interactions in mercury. *Fluid Dyn. Res.* **40** (7-8), 510–520.

TALEYARKHAN, R. P., WEST, C. D., CHO, J. S., LAHEY, R. T. JR., NIGMATULIN, R. I. & BLOCK, R. C. 2002 Evidence for nuclear emissions during acoustic cavitation. *Science* **295** (5561), 1868–1873.

THOMPSON, L. H. & DORAISWAMY, L. K. 1999 Sonochemistry: science and engineering. *Ind. Engng Chem. Res.* **38** (4), 1215–1249 American Chemical Society.

TONG, R. P., SCHIFFERS, W. P., SHAW, S. J., BLAKE, J. R. & EMMONY, D. C. 1999 The role of 'splashing' in the collapse of a laser-generated cavity near a rigid boundary. *J. Fluid Mech.* **380**, 339–361.

TRYGGVASON, G. 2001 A front-tracking method for the computations of multiphase flow. *J. Comput. Phys.* **169** (2), 708–759.

TURANGAN, C. K., JAMALUDDIN, A. R., BALL, G. J. & LEIGHTON, T. G. 2008 Free-Lagrange simulations of the expansion and jetting collapse of air bubbles in water. *J. Fluid Mech.* **598**, 1–25.

WAGNER, W. & PRUSS, A. 2002 The IAPWS formulation 1995 for the thermodynamic properties of ordinary water substance for general and scientific use. *J. Phys. Chem. Ref. Data* **31** (2), 387–535.

WANG, Y. & CHEN, Y. 2007 Application of piezoelectric PVDF film to the measurement of impulsive forces generated by cavitation bubble collapse near a solid boundary. *Exp. Therm. Fluid Sci.* **32** (2), 403–414.

WENINGER, K. R., CAMARA, C. & PUTTERMAN, S. J. 1999 Energy focusing in a converging fluid flow: implications for sonoluminescence. *Phys. Rev. Lett.* **83** (10), 2081–2084.

WOODWARD, P. & COLELLA, P. 1984 The numerical simulation of two-dimensional fluid flow with strong shocks. *J. Comput. Phys.* **54**, 115–173.

WU, C. C. & ROBERTS, P. H. 1993 Shock-wave propagation in a sonoluminescing gas bubble. *Phys. Rev. Lett.* **70** (22), 3424–3427.

XU, Z., GLIMM, J., ZHANG, Y. & LIU, X. 2007 A multiscale front tracking method for compressible free surface flows. *Chem. Engng Sci.* **62** (13), 3538–3548.

YASUI, K. 1997 Alternative model of single-bubble sonoluminescence. *Phys. Rev.* E **56** (6), 6750–6760.

VAN LEER, B. 1977 Towards the ultimate conservative difference scheme. IV. A new approach to numerical convection. *J. Comput. Phys.* **23** (3), 276–299.

VAN LEER, B. 1979 Towards the ultimate conservative difference scheme. V. A second-order sequel to Godunov's method. *J. Comput. Phys.* **32**, 101–136.

https://doi.org/10.1017/jfm.2012.132 Published online by Cambridge University Press